Received: 10 November 2022 | Revised: 12 April 2023 | Accepted: 12 April 2023

DOI: 10.1111/jace.19157

Journal of the American Ceramic Society

RESEARCH ARTICLE

Effects of magnesium on the structure of aluminoborosilicate glasses: NMR assessment of interatomic potentials models for molecular dynamics

Marco Bertani[1,2] | **Nicolas Bisbrouck**[3] | **Jean-Marc Delaye**[3] | **Frédéric Angeli**[3] | **Alfonso Pedone**[1] | **Thibault Charpentier**[2]

[1]Department of Chemical and Geological Sciences, University of Modena and Reggio Emilia, Modena, Italy

[2]Université Paris-Saclay, CEA, CNRS, NIMBE, Gif-sur-Yvette, France

[3]CEA, DES, ISEC, DPME, Université de Montpellier, Marcoule, Bagnols-sur-Cèze Cedex, France

Correspondence
Thibault Charpentier, Université Paris-Saclay, CEA, CNRS, NIMBE, 91191 Gif-sur-Yvette cedex, France.
Email: thibault.charpentier@cea.fr

Funding information
French Alternative Energies and Atomic Energy Commission (CEA); Electricité de France (EDF); Grand Equipement National de Calcul Intensif (GENCI), Grant/Award Numbers: DARI-A0070906303, DARI-A0110906303

Editor's Choice
The Editor-in-Chief recommends this outstanding article.

Abstract

Classical molecular dynamics simulations have been used to investigate the structural role of Mg and its effect when it is incorporated in sodium aluminoborosilicate glasses. The simulations have been performed using three interatomic potentials; one is based on the rigid ionic model parameterized by Wang et al. (2018) and two slightly different parameterization of the core–shell model provided by Stevensson et al. (2018) and Pedone et al. (2020) The accuracies of these models have been assessed by detailed structural analysis and comparing the simulated nuclear magnetic resonance (NMR) spectra for spin active nuclei (^{29}Si, ^{27}Al, ^{11}B, ^{17}O, ^{25}Mg, and ^{23}Na) with the experimental counterparts collected in a previous work. Our simulations reveal that the core–shell parameterizations provide better structural models. In fact, they better reproduce the NMR spectra of all the investigated nuclei and give better agreement with known experimental data. Magnesium is found to be five coordinated on average with distances with oxygen in between a network modifier (like Na) and an intermediate network formed (like Al). It prefers to lay closer to three-coordinated B atoms, forming B–NBO bonds, with respect to Si and especially Al. This can explain the formation of AlO_5 and AlO_6 units in the investigated Na-free glass, together with a Si clusterization.

KEYWORDS
borosilicate glass, GIPAW, magnesium, molecular dynamics, nuclear magnetic resonance

1 | INTRODUCTION

Aluminoborosilicate glasses are key technological materials that find application in many fields, such as biomedical materials,[1] protective screens for electronic devices,[2,3] chemical and heat resistant glass containers (such as Pyrex glass[4]), glazes for ceramics,[5] and nuclear waste confinement.[6–9] As for the latter, several structural studies[10–12] have been performed to understand the structural effects of the major cations of vitreous matrices on the glass chemical durability in the aim of a deep geological disposal.[13] Some of the vitrified high level wastes deriving

from nuclear plants in the United Kingdom (Magnox)[14–16] and France (AVM)[17,18] contain a non-negligible amount of magnesium oxide (almost 5.90 wt% and between 2.5 and 7.5 wt%, respectively[17]) deriving from the coating of non-enriched metallic uranium fuel bars.[19] The role of this alkaline-earth element in the structure of glasses is still subject of debate[15,20–22] because of its low coordination and short bond distance that put it on the edge between a network modifier and an intermediate network former. Depending on the pH of the leaching solution, the incorporation of Mg in glass may enhance its alteration due to the formation of secondary phases that modify the concentration and properties of the alteration layer.[19,23] Thien et al.[17] stated that Mg has two main antagonistic effects on the dissolution rate of aluminoborosilicate glasses in water, which are the precipitation of aluminous hectorite that consumes Si and increases the dissolution rate, whereas the second is the incorporation of Mg in the gel structure, increasing the surface passivation and decreasing the dissolution rate. The effect of the glass composition on these mechanisms is still not clear and an understanding of the structural role of Mg in the glass matrix is fundamental both to unveil its implication on the dissolution behavior as well as modeling its impact.

Because of the lack of long-range order, glass structure is very challenging to be characterized, and local spectroscopies are mostly used to provide structural information at the atomic scale. The most frequently used are Raman, neutron, and X-ray diffraction, and solid-state nuclear magnetic resonance (NMR). The latter has achieved one of the highest level of sophistication, as illustrated by a recent work on Mg aluminoborosilicate glasses.[24]

Complementary to experimental spectroscopies that probe the local glass structure, molecular dynamics (MD) has been increasingly used over time as a reliable tool to predict glass structures at the atomic level.[21,25–32] From such simulations, it is possible to perform an in-depth analysis of structural data, such as bond lengths, angles, ring size distributions, or atomic speciation, which can be prohibitive to access experimentally. The accuracy and reliability of the simulated data critically depend on the potential (or force-field) used in the simulations. Usually, empirical potentials are first validated on the reproduction of known experimental data before the calculated structures can be trustfully used. The choice of the potential depends on the system, on the properties of interest, and on the accuracy and transferability of the available force fields.[33] In literature, several comparative studies can be found that assess the performance of different potentials in the reproduction of the structure and properties of different glass compositions.[28,29,34,35]

Potentials for borate and borosilicate glass systems have been introduced only recently,[27,35–42] and to correctly reproduce the boron anomaly, that is, the dependence of boron coordination with composition, composition dependent parameters for B–O interactions are often required.[43–46]

The present study follows an experimental and a computational investigation[24,47] of six aluminoborosilicate glasses containing four to five oxides (SiO_2, Al_2O_3, B_2O_3, MgO, Na_2O, and CaO). In these works, the structure of the studied glasses was investigated via multinuclear NMR, neutron diffraction, Raman spectroscopy, and with MD simulations. The simulation boxes used in the previous work (5000 atoms) does not allow performing DFT relaxation of the structure followed by DFT NMR calculations. Moreover, some discrepancies between the simulated and experimental structural data raised questions about the overall accuracy of the employed potential.[27,47] As such, the aim of this work is to evaluate three recently developed potentials that rely on fixed parameters (i.e., not composition dependent), in the reproduction of multinuclear NMR data (^{11}B, ^{27}Al, ^{29}Si, ^{17}O, ^{23}Na, and ^{25}Mg), using the MD-GIPAW approach,[48] and structural features in order to unveil the role of magnesium in the structure of aluminoborosilicate glasses. The first tested potential, developed by Wang et al.,[27] is the same employed in the previous work, based on a rigid ion model, for which DFT relaxed structures and NMR simulations were missing. This potential cannot represent the whole rigid ion potentials family and it is known to fail in some compositional regions.[35,46]

The other two potentials rely on a core–shell model[49] and have been originally developed by Tilocca et al.[50] The expansion to borosilicate systems has been performed by Stevensson et al.[36] and has been subsequently modified by Pedone et al.[37] who also introduced the parameters for magnesium and aluminum ions.[25,51,52]

2 | MATERIALS AND METHODS

2.1 | Glass compositions

The composition of the glasses investigated is reported in Table 1. Glasses have been labeled N*x*M*y* as in the original investigation where *x* and *y* represent the rounded nominal percentages of Na_2O and MgO, respectively. The glass series shows a systematic substitution of sodium oxide with magnesium oxide (N26M0, N19M8, N13M13, N8M19, and N0M12), and one complementary calcium-containing glass (N19C8) that was synthesized to compare the effect of calcium and magnesium.

To isolate the impact of Mg in the structure, the Si/Al and Si/B ratio were maintained constant, except for the sodium-free glass (N0M12) for which Si/Al and Si/B ratios had to be decreased by 30% to permit the synthesis of a

TABLE 1 Nominal composition and measured density of the studied glasses.

Glass ID	Chemical composition (%mol)						ρ (g/cm^3)
	SiO_2	B_2O_3	Al_2O_3	Na_2O	MgO	CaO	
N26M0	51.3	14.9	7.7	26.1	–	–	2.505
N19M8	51.2	14.9	7.7	18.7	7.5	–	2.450
N13M13	51.2	14.9	7.7	13.1	13.1	–	2.421
N8M19	51.2	14.9	7.7	7.5	18.7	–	2.412
N0M12	51.3	24.2	12.4	–	12.1	–	2.310
N19C8	51.2	14.7	7.7	18.7	–	7.5	2.511

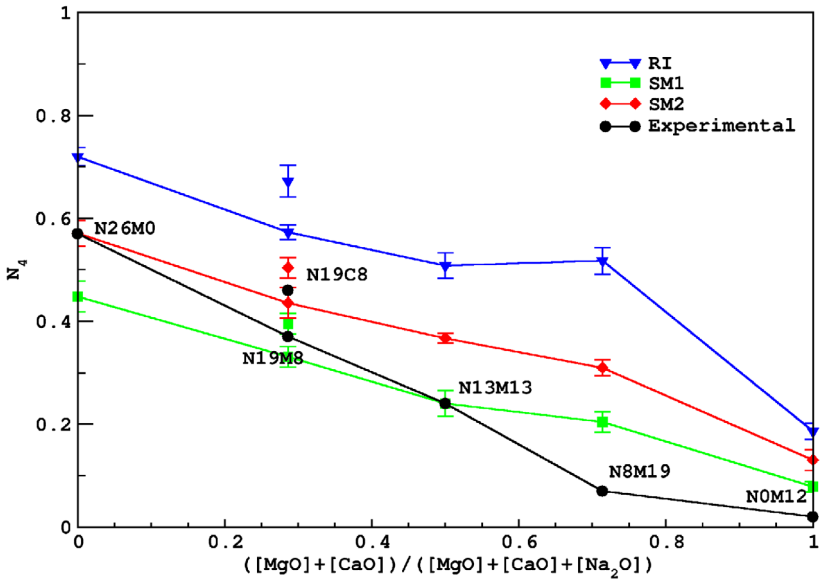

FIGURE 1 Comparison between the BO_4 fraction (N_4) obtained from the simulation with the three tested potentials and the experimental values[24] extracted from ^{11}B MAS nuclear magnetic resonance (NMR) spectra. Note that two N_4 values are reported for N19M8 (Mg) and N19C8 (Ca) at $([MgO] + [CaO])/([MgO] + [CaO] + [Na_2O]) = 0.3$, respectively.

homogeneous specimen (for higher Mg content, a partial crystalline phase was observed).

2.2 | Simulation details

MD simulations were performed using the DL_POLY[53] package with the three potentials. For all the studied glasses and potentials, eight independent simulations of boxes containing ~700 atoms were performed. The system size had to be limited because of the high computational cost of the DFT computations of the NMR parameters, as detailed below. As reported in Figures S1–S3, the comparison of the coordination numbers (for all atoms) with MD simulations performed on five times larger boxes (~3500 atoms) did not show significant differences. All the reported data refer to the average of the values obtained from the independent simulations and error bars indicate the standard deviation.[54]

For all the simulations, the atoms have been randomly positioned in a cubic box with periodic boundary conditions, with edge lengths that reproduce the experimental densities. Details on the simulation boxes are reported in Table S1.

After the MD simulations, the structures (atomic positions and unit cell parameters) have been optimized at the DFT level (details are provided in the Supporting Information [SI]) using the CP2K code.[55] This means that in terms of the medium range structure (characterized by features such as coordination numbers, Q^n speciations and ring size distributions), structures before and after the DFT optimization are equivalent. After the DFT optimization, the differences between the structures generated from different MD potentials only arise from changes in the local arrangement of atoms that defines the medium range structure (as probed by NMR) but bond lengths and bond angles values are determined by DFT (and thus having the DFT accuracy as required for an accurate prediction of the NMR spectra).

2.2.1 | Rigid ion potential

The first potential is a rigid-ion model force-field developed by Wang et al.[27] (referred to as RI potential from hereafter). It is based on two-body interactions, between cation-oxygen and oxygen–oxygen pairs, described by a long-range Coulombic term and a short-range Buckingham type

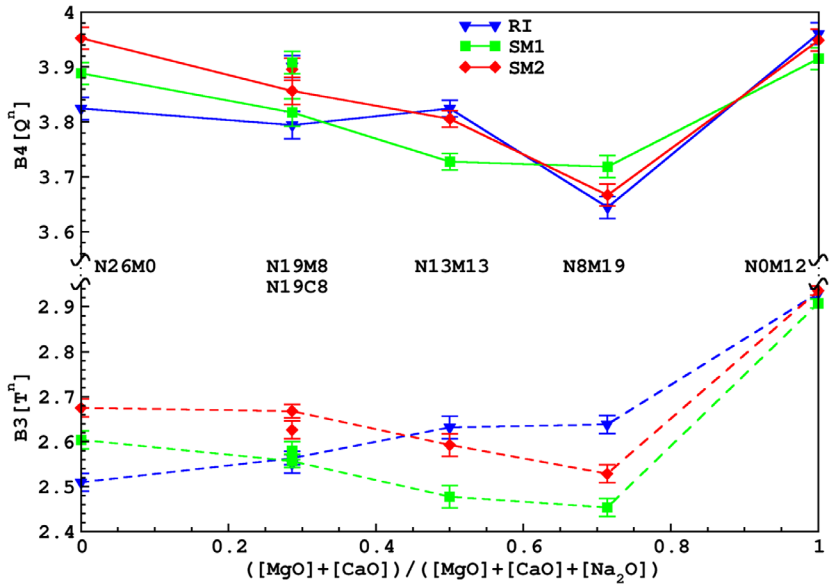

FIGURE 2 Mean number of bridging oxygen atoms (n) linked to BO_4 (Q^n) and BO_3 species (T^n), respectively.

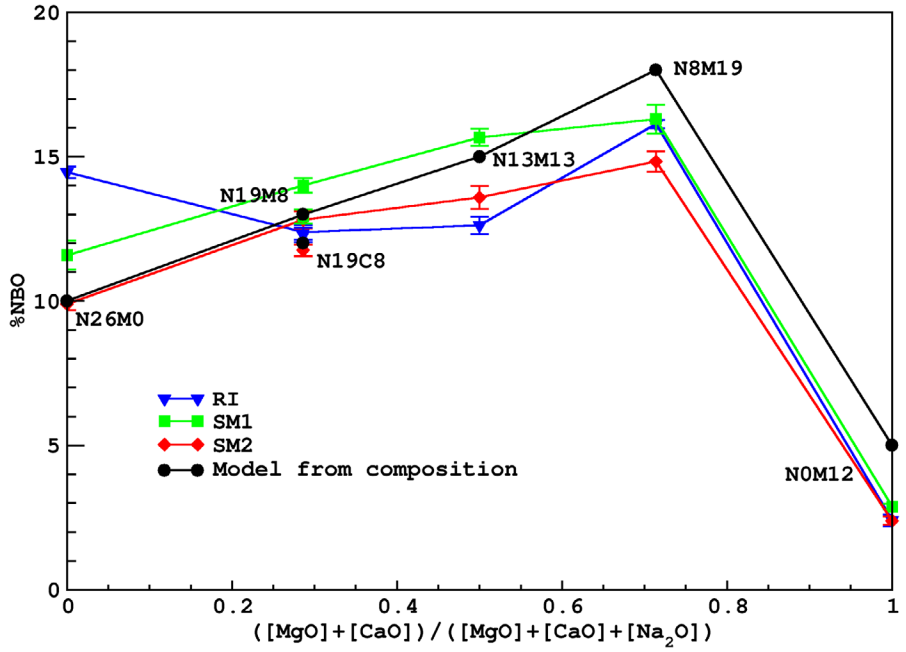

FIGURE 3 Comparison of variation of NBO percentage values with the composition of the studied glasses computed with Equation (2) and calculated from the molecular dynamics (MD) simulations.

interaction. This is expressed in the following equation:

$$U_{ij}(r_{ij}) = \frac{z_i z_j}{r_{ij}} + A_{ij}\exp\left(-\frac{r_{ij}}{\rho_{ij}}\right) - \frac{C_{ij}}{r_{ij}^6} \qquad (1)$$

where r_{ij} is the interatomic distance between atoms i and j, zi and z_j are the partial charges of atom i and j, respectively, and A_{ij}, ρ_{ij}, and C_{ij} are the short-range potential parameters for the ij pairs. The value of the parameters can be found in the original paper.[27] This potential was originally developed starting from the Guillot–Sator framework[56] and makes use of simple formula and fixed parameters with the aim to improve its transferability and computational efficiency at the cost of lower accuracy.[29]

A timestep of 0.5 fs was used, with cut-off radii for both the long and short-range interactions of 10 Å. The Ewald summation method[57] was employed to calculate the Coulombic contribution.

The initial (random) configuration was first equilibrated at 3500 K for 100 ps in the NVT ensemble, to ensure that the

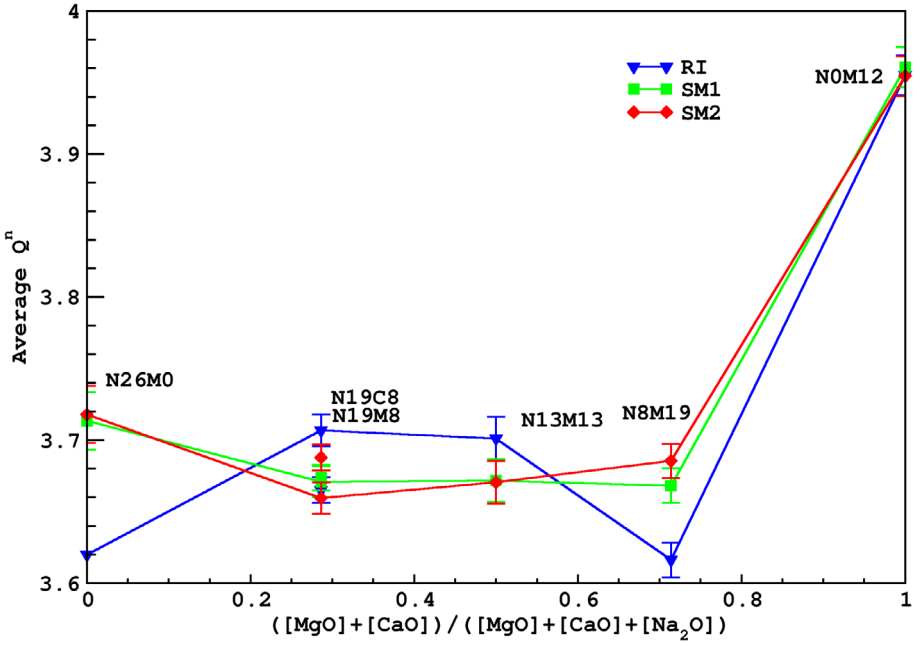

FIGURE 4 Average Si[Q^n] distribution for the studied glasses obtained with the three considered potentials.

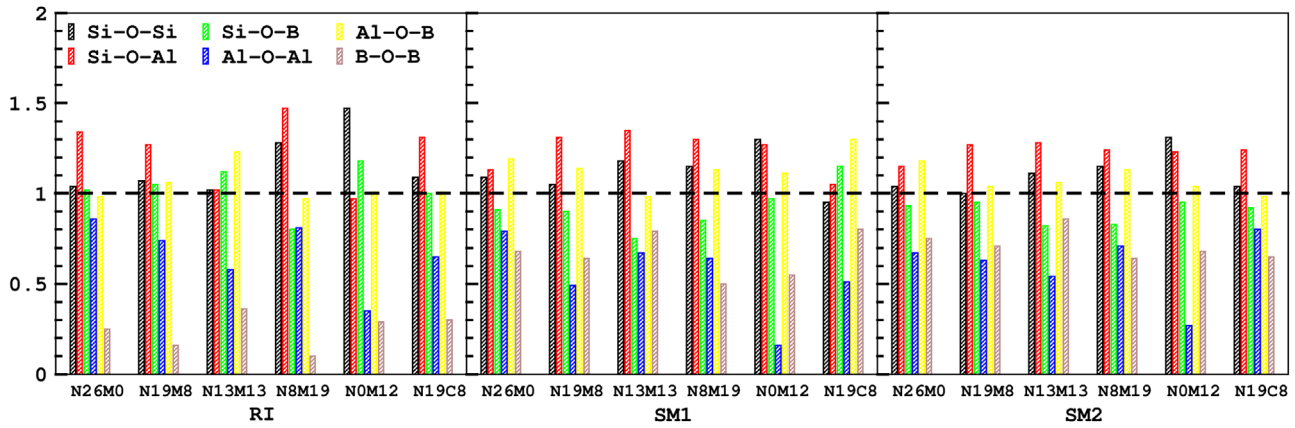

FIGURE 5 Ratio between the %T–O–T (T = Si, Al, and B) bridges obtained by molecular dynamics (MD) simulations and from a complete random structure, for all the studied compositions.

system reached the liquid phase. After this equilibration step, the systems were cooled down to 300 K with a quench rate of 4 K/ps, in steps of 100 K. At each temperature, the system was kept in the NVT ensemble for 10 ps and in the NVE ensemble for 30 ps. The Nosé–Hoover thermostat[58,59] has been applied with a relaxation constant of 1 ps. As discussed in the SI, this procedure resulted in structures with a fictive temperature T_g ranging from 1000 to 1500 K (Figure S4). Investigation of the impact of the quench rate on coordination numbers over a range of quench rate varying from 0.5 to 10 K/ps is reported in Figure S5 and did not reveal significant variations for the studied models in term of speciations. A more detailed analysis of the quench rate on the simulated NMR spectra is out of the scope of the present work and is left for future studies.

2.2.2 | Core–shell potential and its modifications

The potential developed by Stevensson et al.[36] (SM1 potential from hereafter), which is an extension of the Tilocca[50,60] potential, is based on the shell model proposed by Dick and Overhauser.[49] In this model, the total charge

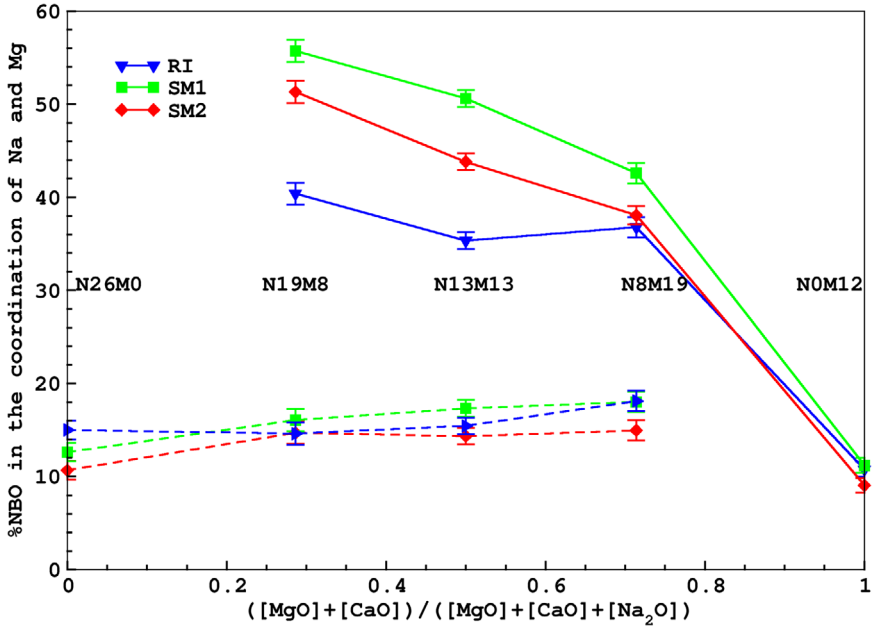

FIGURE 6 %NBO in the first coordination sphere of Mg (solid lines) and Na (dashed lines).

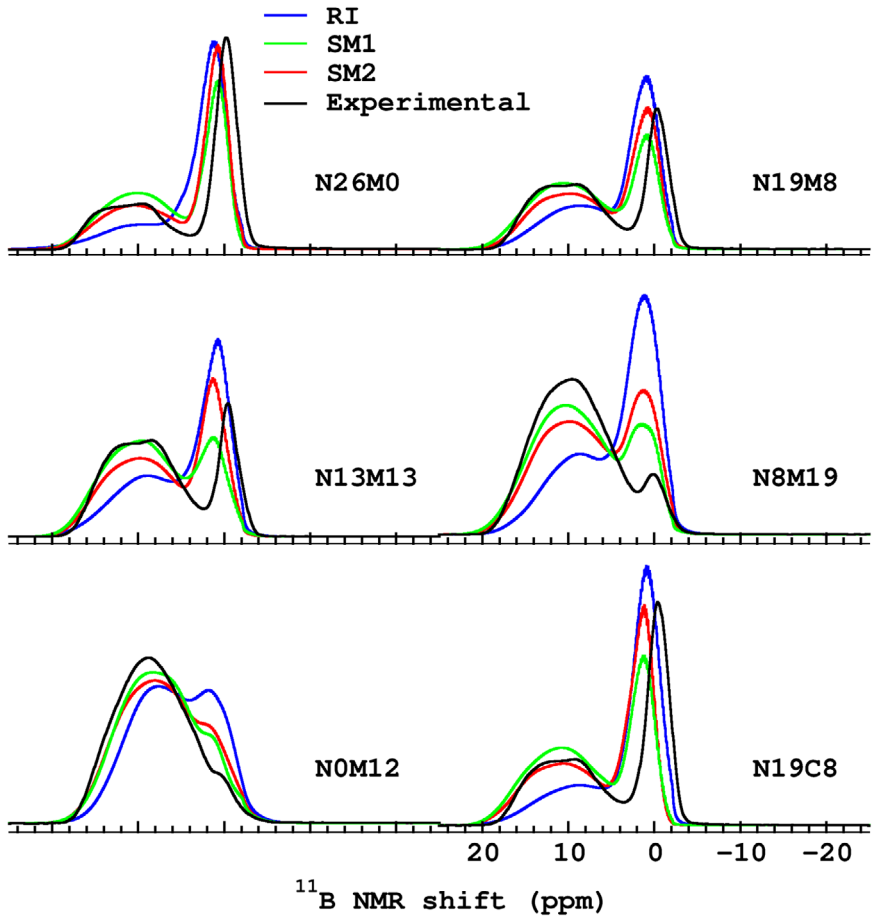

FIGURE 7 Experimental[24] and simulated ^{11}B MAS NMR spectra of the studied glasses.

Z of the oxygen ions is split between a massive core of charge $Z + Y$ and a massless shell of charge $-Y$. The core and the shell are coupled by a harmonic spring. The potential is composed by two-bodies Coulomb and Buckingham potentials that describe the long and short-range interactions (see Equation 1) and a repulsive term (D/r^{12}) that is needed to avoid unphysical overlap of atoms at high temperature.

The original parameterization by Stevensson et al. performed surprisingly well for a wide range of glass

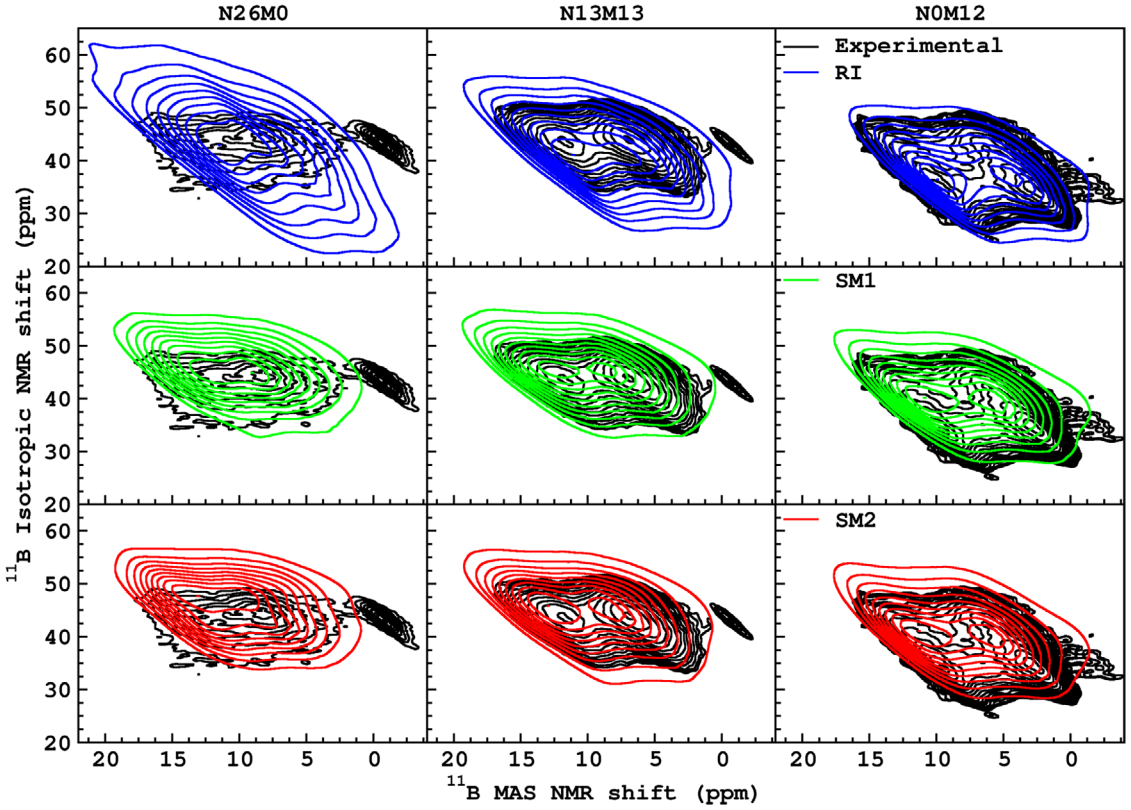

FIGURE 8 Simulated and experimental[24] ^{11}B [BO_3] MQMAS NMR spectra of N26M0, N13M13, and N0M12 glasses.

FIGURE 9 Simulated and experimental[24] ^{11}B [BO_4] MQMAS NMR spectra of N26M0 and N13M13 glasses.

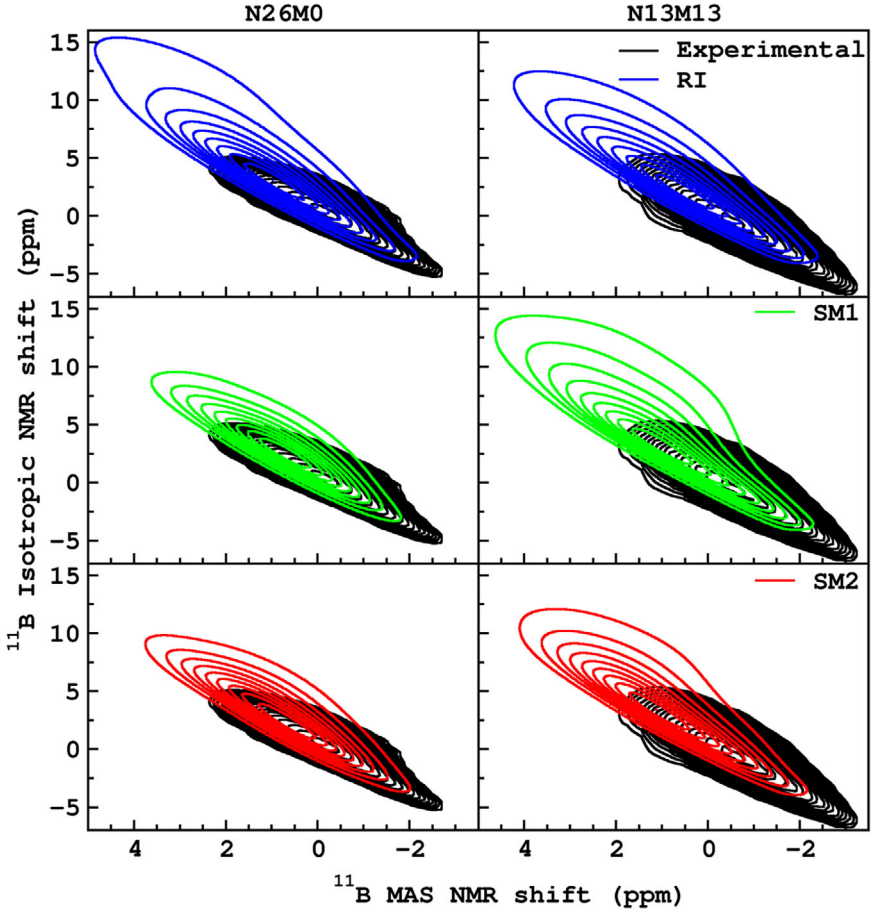

compositions[36,61] with exception of those presenting a predominance of BO_4 that was underestimated.[35] To reproduce better the partitioning of BO_3 and BO_4 species in glass composition with high $K = [SiO_2]/[B_2O_3]$ values the B–O parameters was modified by Pedone et al. in a subsequent work.[37] All parameters can be found in the original papers.[36,37] These two different parameterizations are compared in this work and they will be referred to as SM1 and SM2 potential from hereafter. The Mg–O parameters were not present in the original work of Stevensson et al.[36] thus the ones developed by Pedone et al.[25] have been used for the two core–shell parameterizations considered here.

The cutoff for the Coulomb interactions, calculated with the Ewald summation method,[57] was fixed at 12 Å, whereas for van der Waals interactions a cut off of 7 Å was used. All the core–shell simulations (SM1 and SM2) were performed in the NVT ensemble only, using Nosé–Hoover thermostat with a relaxation constant of 1 ps, because the simulation in the microcanonical ensemble at high temperature was unstable and leaded the system to crash because of the increase of the shell temperature. In fact, in all the previous MD simulations with the shell model,[25,28,32,37] the NVT ensemble was used at high temperature. Tilocca et al.[50] used the NVE only at low temperature. The timestep was lowered to 0.1 fs to deal with the shell fluctuations.

The simulation procedure with the SM potentials was the following. It started with an equilibration at 2500 K for 100 ps to melt the structures and then cooled to 300 K with a quench rate of 10 K/ps. The quench was performed by decreasing the temperature in steps of 100 K every 10 ps in the NVT ensemble. After the quench, the system was equilibrated at 300 K for 20 ps. Similarly to RI models, variation of the quench rate 0.5–10 K/ps did not lead to significant variation of the speciation of atoms, with respect to fluctuations observed from one simulation to another, using the same conditions (see Figure S6).

2.3 | NMR simulations

NMR DFT calculations were performed on the MD structural models, after a preliminary DFT optimization of their structure (atomic positions and cell parameters) with the CP2K code.[55] This code was found to be most efficient for these ~700 atoms models. The NMR parameters were then computed using the GIPAW[62,63] approach as implemented in the VASP program (version 5.3).[64] The generalized gradient approximation PBE[65] functional was employed using the PAW pseudopotentials provided with VASP. However, as highlighted in recent works[66] it was found that the energy of the empty 3d Ca orbital needed to be shifted by 5.1 eV (otherwise causing an overestimation of the hybridization with O 2p orbitals) in order to predict correctly the ^{17}O NMR shift.[67] Outputs of the DFT-GIPAW calculations (i.e., magnetic shielding and electric field gradient—EFG—tensors computed for each atom in the structure) were processed with the in-house code fpNMR program. Notably, the Kernel Density Estimation approach is necessary for simulating two-dimensional MQMAS NMR spectra[54,68] to overcome the limitations due to the small number of environments. The pseudopotential details can be found in Table S2. Cutoff radii used for the structural analysis (coordination numbers and atomic speciations) are given in Table S3.

3 | RESULTS

In this section, the results of the simulations performed using the RI, SM1, and SM2 potentials will be presented with the aim of assessing which one provides the best structural models for the studied compositions. The direct comparison of the NMR spectra of spin active nuclei (^{11}B, ^{17}O, ^{23}Na, ^{25}Mg, ^{27}Al, and ^{29}Si) constituting the glass computed using the MD-GIPAW approach[48] with the experimental ones[24] will provide a strong validation of the underlying structural models. Comparison of experimental and simulated neutron diffraction spectra and their deconvolution are reported in Figures S7–S9. More data about network modifier coordination numbers and bond distances can be found in the SI.

3.1 | Atomic speciation

3.1.1 | Boron speciation

The boron coordination is a crucial structural feature that affects the macroscopic properties of glasses,[69–71] such as thermal and mechanical properties. Boron can be found in glasses as three (BO_3) or four (BO_4) coordinated species. In simple borate and borosilicate glasses, the fraction of BO_4 (N_4 from hereafter) depends on the amount of modifier oxide and SiO_2 in a nonlinear way.

As the aim of this work is to understand the role of Mg and which potential can better reproduce N_4, data will be reported as a function of the ratio $([MgO] + [CaO])/([MgO] + [CaO] + [Na_2O])$.

Figure 1 shows a comparison of the predicted N4 of all the studied glasses with the three evaluated potentials and experimental values extracted from the deconvolution of the 11B MAS NMR experiments.[24]

Globally, the core–shell models provide better N4 fractions with respect to the rigid-ion model potential tested here. The latter gives a clear overestimation of the boron coordination (15%–40% more BO4 than experiments), even if the overall decreasing trend of N_4 with Mg content increasing is well respected. The RI potential is known to overestimate the N4 fraction in glasses with high R ($[M(2)O]/[B_2O_3]$) values while it gives excellent results for glasses at low content of modifier oxides,[29,35] and this trend is confirmed here. We found a mean absolute error (MAE) of 24.7% and a maximum positive error of 44.7% on the N8M19 glass.

Comparing the two boron parameterizations of the core–shell potential, SM1 gives the best agreement, showing excellent values and trend, with a MAE of 6.5% and a maximum error of 13.4% on the N8M19 glass, whereas SM2 gives a MAE of 10.0% and a maximum error of 24.0% on the N8M19 glass. The SM1 potential better reproduces the boron coordination for glasses when the BO_3 speciation is dominant. In contrast, for the N26M0 glass, where 57% of boron are in BO_4 units, the SM1 potential underestimates it by 12.3%, whereas SM2 gives a nearly perfect agreement, confirming its better accuracy for glasses with high BO_4 content.

Figure 2 shows the mean number of bridging oxygen (BO) atoms *n* in BO_4 (denoted as Q^n) and BO3 (denoted as T^n) units, respectively, for the investigated glasses. Because of the negative charge of BO_4 unit and the charge neutrality of BO_3 one, only the latter units are generally considered candidate for forming NBO atoms.[72,73] For this reason, the average Q^n (BO_4) value should be as close as possible to 4. The SM2 potential seems to perform better than the others on this point. In fact, it predicts the higher Q^n speciation (i.e., less NBO on BO_4) value for all the glasses except N8M19, for which SM1 gives the highest value. SM1 gives, in general, lower Q^n and T^n species than its modified version, showing a clear preference of the NBO formation on boron units that will be further discussed later. The RI potential predicts the lowest Q^n for N26M0, N19M8, and N8M19 while it gives better results for the other glasses. The substitution of Mg with Ca does not significantly impact the Q^n and T*n* distributions, even if a slight increase of Q^n species is observed. It is possible that, at the N19M8/N19C8 compositions, Mg and Ca behave similarly or that the potentials are not able to catch all the specificities of Ca versus Mg. In general, the substitution of Na with Mg, from N26M0 to N8M19 (N0M12 has different composition) favors the formation of NBO on BO_4, probably because of the double positive charge of Mg that can compensate a NBO on a negative unit. The evolution for BO_3 is more mitigated, but the two SM potentials follow the same trend.

TABLE 2 Mean values of $\%AlO_5$ calculated from the molecular dynamics (MD) simulations with the three considered potentials.

$\%AlO_5$	RI	SM1	SM2
N26M0	7.6 (3.4)	1.6 (2.3)	0.8 (1.4)
N19M8	8.9 (4.8)	0.8 (1.4)	1.2 (1.5)
N13M13	9.0 (5.0)	2.0 (2.2)	2.0 (2.2)
N8M19	9.3 (3.8)	5.7 (4.9)	2.7 (2.8)
N0M12	18.0 (3.7)	5.2 (1.6)	4.9 (2.5)
N19C8	12.8 (6.0)	1.6 (1.6)	2.3 (1.4)

Note: Standard deviation values are given in parentheses.

3.1.2 | Aluminum speciation

Aluminum is usually found to be four-coordinated and fully polymerized (i.e., no NBO) at exception of glass compositions poor in modifiers or when high-field cations, like Mg, are present.[24,74–76] In these cases, a non-negligible amount of AlO_5 and AlO_6 is present. Such higher coordination states of aluminum can be well resolved in ^{27}Al MAS NMR experiments, where signals at lower chemical shifts are present, around 30 and 0 ppm, for AlO_5 and AlO_6, respectively (versus 60 ppm for AlO_4).

MAS NMR experiments[24] show that aluminum is completely four coordinated for all compositions except N0M12, where 16% and 6% of AlO_5 and AlO_6 are present, respectively.

As reported in Table 2, the RI potential predicts a significant amount of five-folded aluminum, which is not observed in NMR experiments. This could be related to a too high interaction between magnesium and aluminum. The highest percentage is found in N0M12, which is consistent with experiments. None of the potential predict the presence of AlO_6 speciation.

The two core–shell potentials (SM1 and SM2) both predict a very low percentage of AlO_5, which slightly increases for N0M12. It should be pointed out that not all the independent MD structures contain AlO_5 units (except for N0M12). This explains the standard deviations higher than the average values. These low $\%AlO_5$ values are ascribed to the inclusion of a strong O–Al–O three body interaction in our SM potentials that constraints aluminum to have a tetragonal coordination polyhedron. A new parameterization of this interaction could be of great interest to better reproduce the aluminum speciation in glasses where highly coordinated Al is present. Nevertheless, the presence of a significant amount of AlO_5 only in N0M12 glass, which is indeed experimentally the only one that contains five and six coordinated Al, is an indication of the good core–shell potentials performance.

Because of the global negative charge carried by AlO_4 units, aluminum is usually fully polymerized, that is, with-

out NBO, so it has to be present as Q^4 species only. The two SM potentials give a %Al[Q^4] value that is always higher than 96%. As for the RI potential, it predicts however a non-negligible amounts of Al[Q^3] (i.e., AlO_4 with one NBO) which ranges from 1.8% in N0M12 to 9.4% in N8M19. Complete data are reported in Table S4. Such a high value can explain the larger deviation of %BO_4 observed specifically for this glass composition (Figure 1). This effect can be ascribed to a too high interaction between Al and Mg that will be further investigated in the next sections.

3.1.3 | Oxygen speciation

If the percentage of NBO in the glass series could not be extracted unambiguously from experiments,[24] it can be estimated from the glass composition using the following equation:

$$\%\mathrm{NBO} = 100 \times \frac{2\times([\mathrm{Na_2O}]+[\mathrm{CaO}]+[\mathrm{MgO}]-[\mathrm{Al_2O_3}]-[(\mathrm{B\,[IV]})\times \mathrm{B_2O_3}])}{2\times[\mathrm{SiO_2}]+[\mathrm{Na_2O}]+[\mathrm{MgO}]+[\mathrm{CaO}]+3\times([\mathrm{Al_2O_3}]+[\mathrm{B_2O_3}])} \quad (2)$$

In Equation (2), as five-coordinated aluminum is present only in one glass and in a minor quantity, the assumption has been made that all aluminum units are coordinated by four BOs (i.e., 100% Al[Q^4]). Figure 3 shows a comparison between the %NBO calculated from MD simulations with the one predicted by Equation (2).

The trend given by Equation (2) is well reproduced only by the SM potential. The RI one gives the worst results showing a clear overestimation of the %NBO in Mg-free glass followed by a general underestimation in all the other compositions.

The two core–shell potentials perform similarly. The SM1 slightly overestimates the %NBO in glasses with low MgO content (so at higher BO_4 content), where the SM2 performs better. When the Mg contribution is predominant, and the N_4 fraction decreases, SM1 gives the best results. The Na-free glass (N0M12) shows a very little amount of NBO that is well reproduced (even if underestimated) by all the potentials. In this glass, the network polymerization is very high, and a non-negligible amount of three-clustered oxygens (TO) have been produced in the simulations, which are 10.7%, 6.3%, and 5.6% with RI, SM2, and SM1 potentials, respectively (see Table S5).

The almost complete absence of NBO in N0M12 glass and the very low N_4 fraction would suggest that Mg acts exclusively as a charge compensator for AlO_4^- units, but the presence of small quantities of $AlO_{5/6}$ and TO does not support such a mechanism. The average coordination number of Mg, which ranges from 5 to 5.3, and the Mg–O distance (1.99–2.25 Å), which is in between the Al–O and Na–O distances (Tables S6 and S7) that are obtained with all potentials, support the idea that Mg have a behavior in between a network modifier and intermediate network former. This seems particularly true for the N0M12 glass, where the Mg–O distance is the lowest of the glass series for all the potentials. T–O–T angles (T = Si, B, and Al) are reported in Table S8.

3.1.4 | Silicon speciation

The three considered potentials predicts, for all the studied glasses, only four coordinated silicon.

The average value of n (i.e., number of BO) in Q^n distribution of silicon is reported in Figure 4.

The two core–shell potentials give almost identical values for all the glasses (note that they share the same Si parameters) with an average Q^n speciation that is almost constant (around 3.65) for all glasses except for N0M12, where it is close to 4, following the %NBO trend (Figure 3). The RI potential shows a Si[Q^n] trend that follows the %NBO one, showing lower values for N26M0 and N8M19 with respect to N19M8 and N13M13 and very high polymerization (i.e., high Q^n) in N0M12. The substitution of Mg with Ca does not show a significant impact. In fact, with RI potential the Si[Q^n] decreases, while with SM2 it slightly increases and with SM1 it remains constant. Globally, in all Na-bearing models, silicon tetrahedra are relatively in highly polymerized, with a NBO/T value of 0.3–0.4. With Mg only (N0M12), the value significantly decreases, less than 0.1.

3.2 | Bond preferences

In this section, the variations of T–O–T (T = Si, Al, and B), T–NBO, and M–NBO (M = Mg, Na, and Ca) amount in the simulated structures are presented and the preference for the formation of specific bond/coordination is discussed. Primary ring structure distributions have also been computed and are reported in Figure S10.

3.2.1 | T–O–T bridges (T = Al, B, and Si)

The percentage of each T–O–T bridge, normalized to the total amount of BO, is reported in Table S9 for all glasses, simulated with the three potentials.

The Löwenstein avoidance rule[77] for Al, stating that in aluminosilicate glasses the formation of Al–O–Al is unfavorable because of the negative charge of AlO4 units, can be extended to boron in the four-coordinated state.[78,79] Accordingly, in the studied glasses, the percentage of Al–O–Al should be close to 0, and the amount of B–O–B and B–O–Al limited by the presence of BO_4.

It is interesting to compare the amount of T–O–T bridges in the structures simulated with MD with the amount predicted from a complete random structure with the same composition. Figure 5 reports the ratio of the percentage of each T–O–T in the simulated structure and in the random one. When this value is clearly higher than 1 for homo- (i.e., Si–O–Si, Al–O–Al, and B–O–B) bridges, it indicates a possible clusterization with T-rich regions in the glass.

With all the potentials, Si–O–Al bonds are favored with respect to Al–O–Al and Si–O–Si thus following the Löwenstein rule, except for the N0M12 glass where Si–O–Si is predominant. The increasing percentage of Si–O–Si, which is evident in the Na-free glass, can be related to a Si clusterization, that is, a formation of pure silicate network or Si-rich regions in the glass structure. This is agreement with the interpretation of ^{29}Si and ^{17}O NMR experiments.[24] The RI potential provides the lowest %B–O–B, probably because of the higher %BO_4 units that tends not link with each other because of their negative charge.

The two SM potentials also show a Si–O–B ratio <1 and Al–O–B ratio >1. The former could be the bridge that "brakes" when the Si segregation is present, generating the latter. Interestingly, the relative stabilities of these two bridges reflect the acid-basic properties of the oxides: SiO_2 and B_2O_3 are acids, whereas Al_2O_3 is amphoteric.

So globally, we observe preferential Si–O–Si and Si–O–Al linkages, and to a less extent Al–O–B, whereas Al–O–Al and B–O–B appear to be less favored. The substitution of Mg with Ca does not give rise to significant variations, except when using SM1 for which Si–O–Al decreases and Si–O–B and Al–O–B increase.

3.2.2 | T–NBO preferences (T = Al, B, and Si)

Non-BO atoms are generated by modifier cations and cause a depolymerization of the glass network. Because of bearing a global negative charge, as discussed previously, the formation of NBO on AlO_4 and BO_4 is very unfavorable and the simulation should generate the lowest possible amount of BO_4–NBO and AlO_4–NBO linkages.

The distribution of the NBO present in the simulation boxes on the different network former cations, renormalized with the total number of NBOs, is reported in Table S10. None of the potentials predict NBO on AlO_5 units when they are present (only N0M12 for the two SM and in all the compositions for RI). The RI potential always predicts a non-negligible amount of NBO linked to AlO_4 and BO_4, which seems to be a general deficiency of RI type potential.

SM1 and SM2 potentials predict a very low %NBO on AlO_4. Furthermore, as is shown in Figure 2, NBOs are preferentially generated on BO_3 with respect to BO_4, even when the N_4 fraction is predominant. SM2 potential predicts, in general, less B–NBO bonds, probably because of the higher A_{B-O} and ρ_{B-O} Buckingham parameters that lengthen the B–O bonds (see Tables S6 and S7).

To better understand the probability of the formation of NBO on the different network former cations, we normalized the amount of NBO–T over the amount of T atoms in the simulation boxes ($R_{T1/T2}$ from hereafter) as it follows:

$$R_{T1/T2} = \frac{N^{\circ}_{T1-\mathrm{NBO}}/N^{\circ}_{T1}}{N^{\circ}_{T2-\mathrm{NBO}}/N^{\circ}_{T2}} \quad (3)$$

where $N^{\circ}_{T1\text{-}NBO}$ is the amount of $T1$–NBO bonds, and N°_{T1} is the amount of $T1$ atoms in the simulation box. If $R_{T1/T2} > 1$ the formation of NBO on $T1$ is favored with respect to $T2$.

As reported in Table 3, all potentials show a clear preference for the NBO to form on BO_3 and SiO_4 rather than on AlO_4, but, following the consideration made above, the RI potential gives the highest $R_{Al/Si}$ and $R_{Al/B}$ values.

The $R_{Si/B}$ values show a decreasing trend for all the potentials and a higher value for N19C8 than N19M8 is predicted only with SM1. It is possible, that Mg atoms lay closer to boron with respect to Na ones (see Na–B and Mg–B radial distribution functions in Figure S11), generating NBO on BO_3 instead of charge compensating BO_4^-. This is confirmed by the M–NBO–T (M = Na, Mg, and Ca; T = Si, Al, and B) coordination numbers reported in Table S11: Mg creates an increasing amount of NBOs on BO_3. The latter consideration seems true in all the glass series except N0M12 glass, where the preference of Mg for B is maintained, but almost no NBOs are present. The $R_{Si/B}$ values are higher with SM2 than SM1 following the considerations made above.

The $R_{BO3/BO4}$ decreases along with the glass series for all the potentials but it never falls under 1, favoring the

TABLE 3 Preference for T–NBO formation (T = Al, B, and Si) expressed as $R_{T1/T2}$.

RI				
Glass/$R_{T1/T2}$	**Al/Si**	**Al/B**	**Si/B**	**BO_3/BO_4**
N26M0	0.33	0.64	1.93	2.91
N19M8	0.20	0.24	1.17	2.12
N13M13	0.28	0.30	1.08	2.15
N8M19	0.55	0.94	1.72	1.15
N0M12	0.11	0.09	0.82	1.78
N19C8	0.07	0.07	1.03	4.52
SM1				
Glass/$R_{T1/T2}$	**Al/Si**	**Al/B**	**Si/B**	**BO_3/BO_4**
N26M0	0.01	0.02	1.06	3.55
N19M8	0.04	0.03	0.92	2.43
N13M13	0.04	0.03	0.71	1.91
N8M19	0.05	0.03	0.66	1.98
N0M12	0.00	0.00	0.43	1.10
N19C8	0.07	0.08	1.10	4.57
SM2				
Glass/$R_{T1/T2}$	**Al/Si**	**Al/B**	**Si/B**	**BO_3/BO_4**
N26M0	0.01	0.02	1.68	6.84
N19M8	0.08	0.11	1.35	2.31
N13M13	0.02	0.02	0.99	2.09
N8M19	0.06	0.04	0.74	1.41
N0M12	0.00	0.00	0.73	1.26
N19C8	0.03	0.03	1.31	3.60

formation of NBO in BO_3 with respect to BO_4. The comparison between $R_{BO3/BO4}$ in N19M8 and N19C8 shows that, for all the potentials, the latter is higher. This could mean, even if BO_4–NBO should not be present, that Mg tends to give a higher distortion in the B (and especially BO_4) environment.

3.2.3 | M–NBO preferences (M = Na, Mg, and Ca)

Network modifier cations can act mainly in two ways in aluminoborosilicate glasses. They can compensate the negative charge of AlO_4 and BO_4 structural units (charge compensator), or they can break the network generating NBOs (network modifier). These two behaviors are not mutually exclusive and the same element can act in fact (partially) in both ways in a glass, resulting in the formation of various M–BO and M–NBO *spatial* linkages. To understand the general tendency of these elements to act either as a charge compensator or as a network modifier (or in between) we have reported in Figure 6 the percentage of NBOs in the Na, Mg, and Ca first coordination sphere, whereas the full oxygen coordination is reported in Figure S12.

TABLE 4 $R_{AE/A}$ as calculated with Equation (4).

$R_{Mg/Na}$	RI	SM1	SM2
N19M8	3.44 (0.21)	3.68 (0.14)	3.68 (0.18)
N13M13	2.16 (0.11)	2.44 (0.20)	2.56 (0.15)
N8M19	1.84 (0.17)	1.66 (0.13)	1.80 (0.19)
N19C8[a]	2.79 (0.12)	3.61 (0.14)	3.59 (0.19)

[a] $R_{Ca/Na}$.

Note: Standard deviations are reported in parentheses.

The percentage of NBOs in the coordination sphere of Mg is always higher than Na, independently on the interatomic potentials used. The percentage of NBO on Na does not change significantly along with the series, only a slight increasing trend is observed. As for Mg, the SM potentials, and in particular SM1, gives higher NBO coordination than the RI 1, and predict a decreasing trend when Mg substitutes Na. All the potential give a strong drop for N0M12 that follows the amount of NBO in the glass. The %NBO in the coordination of Na in N19C8 glass is very close to its Mg analogous for all the potentials. The impact of NBOs on the Ca coordination is lower than on Mg. In fact, the amount of NBOs on Ca is 7 and 14% less when the SM1 and SM2 potentials are used, whereas it is 15% less with the RI.

Furthermore, the preference for the formation of NBO given by the alkaline-earth cations with respect to Na is reported in Table 4 as the $R_{AE/A}$ (where *AE* stands for alkaline-earth and *A* for alkaline cations) calculated with the following equation:

$$R_{AE/A} = \frac{N_{NBO}(AE)}{N_{NBO}(A)} \quad (4)$$

where N_{NBO} is the average number of NBOs coordinated by the considered atom. If $R_{AE/A} > 1$ NBOs are preferentially formed on the alkaline-earth cation and vice versa.

The preferential coordination of NBO by Mg with respect to Na is clear for all the glasses. The decreasing trend is given by the increasing quantity of Mg (and decreasing of Na) that cause Mg to coordinate also a higher amount of BO atoms. In the N19C8 glass, NBOs are preferentially coordinated by Ca with respect to Na. The $R_{Ca/Na}$ is always slightly lower than $R_{Mg/Na}$ in the homologous Mg-glass, especially with the RI potential.

A deeper investigation of the preferential coordination of NBO–T (T = Al, B, and Si) by Mg, Na, and Ca has been carried out. In particular, the number of each modifier atoms in the local environment of T–NBO has been computed and normalized. Data are reported in Table S11.

All the potentials show that Mg prefers to coordinate NBO linked to boron and the same preference is observed for Ca. As for the AlO_4–NBO, only RI predicts a non-negligible amount of such bounds and a high amount of Mg has been found in the environment of these NBO oxygens. Probably, this vicinity, given by a too high affinity of Mg with Al obtained with RI potential, could be the cause of the formation of the Al[Q^3] species that should not be present in the studied glasses.

3.3 | DFT simulations of MAS NMR spectra

In this section, ^{11}B, ^{17}O, ^{27}Al, and ^{29}Si MAS NMR spectra computed with the MD structures are compared to their experimental counterparts, obtained at a magnetic field of 11.7 T (except for ^{25}Mg for which a 17.6 T magnetic field was used) and a spinning rate of 12.5 kHz, for all glasses.[24] ^{23}Na and ^{25}Mg MAS NMR spectra are reported in Figures S13–S16. NMR parameters that were extracted from the MD structures are reported in Tables S12–S20.

3.3.1 | ^{11B} MAS and MQMAS NMR spectra

Figure 7 shows the experimental[24] and simulated ^{11}B MAS NMR spectra of the investigated glasses. The spectra are normalized to the same area in order to highlight the difference in the boron speciation (see also Figure 1). Both SM1 and SM2 potentials better reproduce the shape and position of the spectra with respect to the RI one, and in particular of the BO_3 peak (the broader peak at higher chemical shifts). As it has been shown in Sections 3.1.1 and 3.2.2 and previously by Fortino et al.,[35] this can be ascribed to a better reproduction of the BO_3/BO_4 partitioning and to a better description of the boron local environment (especially, the B–O–B bond angle). The region at higher chemical shift of the BO_3 signal is often related to boron atom in ring structures.[80] The systematic underestimation of this region using the RI potential is indicative of a lack in the reproduction of such boron supramolecular structures. The three potentials give different amount of three-coordinated boron in ring structures of different dimensions (Figure S10). The RI potential provides a narrow primary ring distribution centered at 5 (*n*-membered rings are formed by *n* network former element and *n* BO atoms) with an average BO_3-ring size that ranges from 4.8 (N0M12) to 5.5 (N19M8). SM1 gives a broader ring distribution for BO_3, still centered almost at 5 (4.9–5.6), whereas SM2 predicts smaller average ring size from 4.8 (N19M8) to 5.2 (N13M13). The percentage of BO_3 units in 3-membered rings (i.e., boroxol rings) is low (max 8.5%) and generally higher values are found with the shell models, and especially with SM2, except for N0M12 glass where 8.3% of BO_3 are in boroxol rings using RI (7.3% and 6.5% with SM1 and SM2, respectively). These supramolecular boron structures are usually concerned with the high NMR shift of BO_3.[80] No specific dependence of the percentage of BO_3 in boroxol rings on the composition was found.

None of the potentials can perfectly reproduce the separation between the BO_3 and BO_4 peaks, which is often underestimated by the simulations, especially with the RI potential. Such a discrepancy can be indicative of a wrong B–O–T (T = Al, B, and Si) linkages or wrong BO_4 charge compensation mechanism.

Figures 8 and 9 show the ^{11}B 2D MQMAS NMR spectra of BO_3 and BO_4, respectively, for the representative N26M0, N13M13, and N0M12 glasses. For the latter, only the BO_3 spectrum is reported as the experimental %BO_4 is negligible and gives very noisy BO_4 spectra. All spectra can be found in Figures S17–S19.

Experimentally, the BO_3 MQMAS spectra width along the isotropic NMR shift (vertical dimension in MQMAS, this is a dimension free of second-order quadrupolar broadening present in the MAS dimension) increases along the series. These variations mostly reflect an increase of the isotropic chemical shift distribution,[80] thus an increase of the local disorder around the BO_3 units (here, distribution of BO_3–O–T linkages and related bond angles). Interestingly, a second contribution seems to appear at lower chemical shifts when the Mg content increases, as confirmed by the projection of the MQMAS spectra on the isotropic chemical shift dimension (Figure S18). Main features are qualitatively well reproduced by the SM potentials, whereas the RI potential surprisingly gives a decreasing width of the spectra. The latter can better reproduce the position of the peaks, as confirmed by the isotropic projections, and shows very good agreement with experiments when Mg content becomes predominant.

Concerning the BO_4 MQMAS spectra, all potentials predict significantly broader spectra, clearly overestimating the shift in both the MAS and isotropic dimensions. The region of discrepancy between MD models and experimental data is clearly evidenced by these MQMAS spectra. At higher isotropic chemical shift (also higher NMR shift along the isotropic dimension), the width along the MAS dimension is increasing: This reveals that larger quadrupolar interactions are present. Thus, discrepancies mainly results from overestimated quadrupolar interactions, arising from defective prediction of the cationic environment (i.e., charge compensation mechanisms), of NBO and BO_4–O–T linkage. In literature, BO_4 MQMAS spectra show two sites,[81] with slightly different quadrupolar

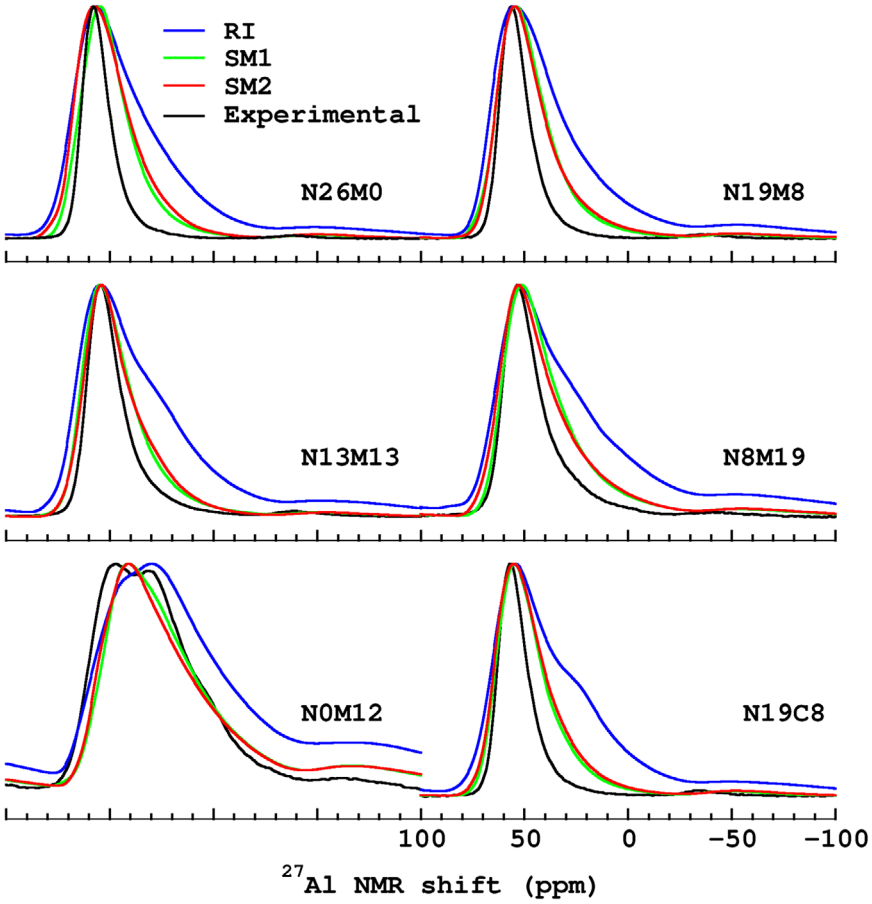

FIGURE 10 Experimental[24] and simulated ^{27}Al MAS NMR spectra of the studied glasses.

interactions that are often attributed to BO_4 bonded to 3Si and 1B or 4Si atoms. The latter is more regular (i.e., less distorted) and has lower quadrupolar interaction than the former. All potentials predict an experimental-like shape of the spectra, with the best agreement given by SM2, even if the signal at lower chemical shift is always underestimated. This systematic shift is currently investigated and may also be resulting from finite temperature effects (such as vibrations of nearby cations).

3.3.2 | ^{27}Al MAS and MQMAS spectra

Figure 10 shows a comparison between the experimental[24] and simulated ^{27}Al MAS NMR spectra obtained with the three considered potentials. The two SM potentials give almost identical spectra so they predict very similar Al environments. Clearly, they better reproduce the shape and the position of the AlO_4 peaks for all the studied glasses, except N0M12, where the position is shifted to lower NMR shifts. The latter, experimentally, shows a double peak with a shoulder at lower chemical shifts that are characteristic of the presence of five- and six-folded aluminum.

The RI potential always predicts a much broader spectra, which can be in part related to the presence of high-coordinated Al (five and six coordinated), and to a higher disorder around Al atoms with respect to the real structure (and to SM structures), and in particular by a higher amount of Mg in the Al environment instead of Na.[24,47,82] In addition, thermal vibrations of cations could have an impact on the observed simulated MAS NMR spectra (theoretically, all simulations are performed at 0 K). Indeed, the time-scale underlying MAS NMR spectra lineshape (from μs to ms) makes it potentially sensitive to thermal events at lower time-scale (mobility of cation) that are not accounted for in the present simulations. Typically, vibrations of cations (Mg, Na, …) can yields an effective EFG (or the quadrupolar interaction) lower that its 0 K value.

It should be emphasized the better reproduction of the MAS NMR spectra by the two SM potentials that predict a lower amount of Mg in the Al environment, versus Na which is the preferred cation for the charge compensation. When Na is not present in the composition (N0M12) Mg is forced to act as a charge compensator (and makes the glass synthesis more difficult as noted in a previous work[24]) causing the reorganization of Al in higher coordinated states.

Figure 11 reports the experimental[24] and simulated ^{27}Al 2D MQMAS NMR spectra of N26M0, N13M13, and

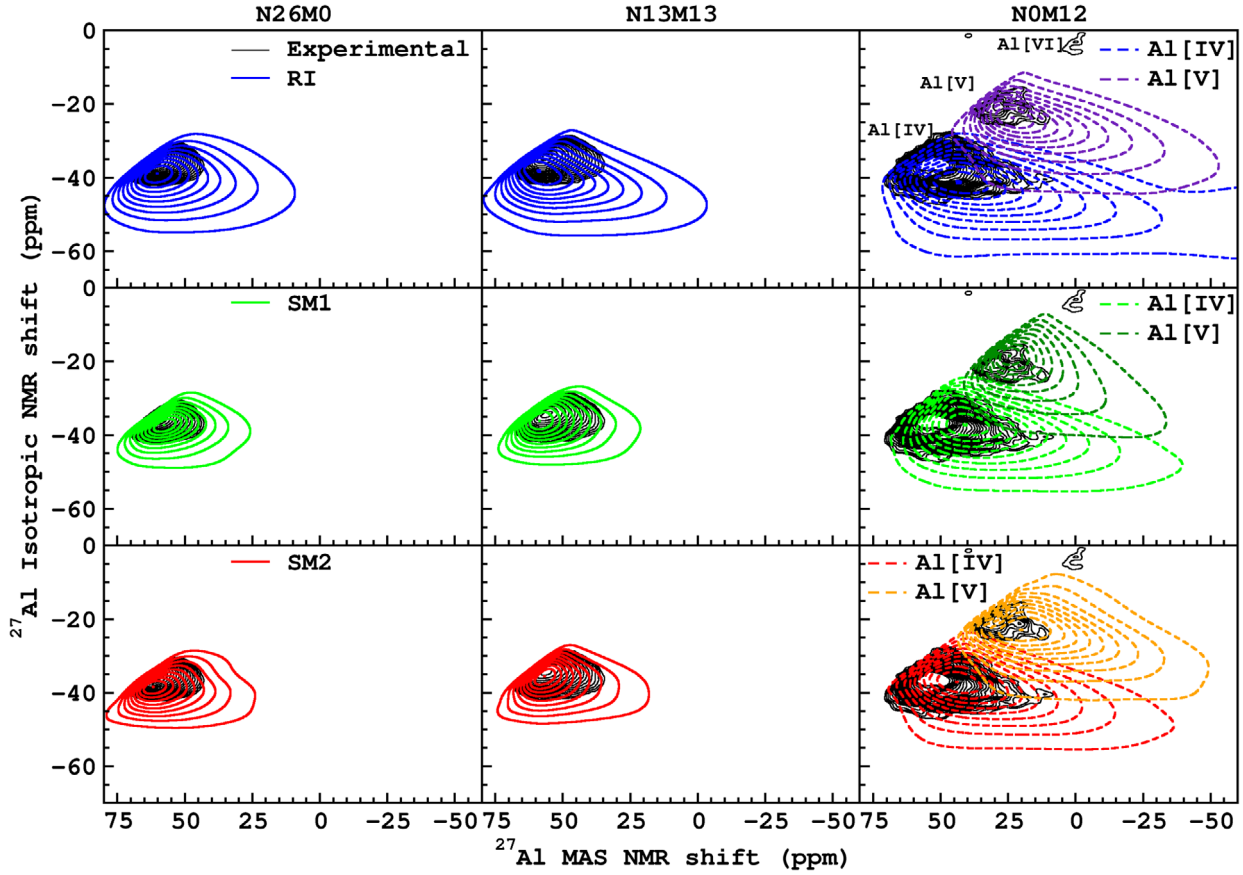

FIGURE 11 Simulated and experimental[24] ^{27}Al MQMAS NMR spectra of N26M0, N13M13, and N0M12 glasses.

N0M12 glasses. The spectra of the full series can be found in Figure S20. As for the Na-containing glasses, only the Al[IV] contribution of the simulated spectra is reported, whereas for N0M12 also the Al[V] is present.

The MQMAS spectra confirm that RI potential gives a more distributed Al environment with respect to SM1 and SM2, thus showing broader spectra. This is particularly evident in N0M12 glass, where the experimental broadening of the Al[IV] signal is extremely overestimated. However, it should be noted that MQMAS spectra have been simulated without the effect of the MQMAS RF pulse sequence that, in contrast to the MAS spectra, severely impacts the lineshape of the MQMAS spectra, due a nonhomogeneous excitation of sites with respect to their quadrupolar interactions. Globally, this leads to a decrease of intensity of sites with larger quadrupolar interactions and thus explains the discrepancies in Figure 11. However, it should be noted that along the isotropic dimension (free of the second-order quadrupolar interactions), SM spectra clearly better reproduces the experiments. This is indicative a better isotropic chemical shift distribution by the SM potential, versus the RI one.

3.3.3 | ^{17}O MAS and MQMAS NMR spectra

As shown in Figure 12, the three studied potentials produce similar ^{17}O MAS NMR spectra. At first glance, the shape and position of the signal for all the studied glasses is very well reproduced indicating that oxygen environment is well reproduced. However, from the experimental 1D MAS NMR spectra it is not possible to distinguish BO and NBO contributions, and the deconvolution of the simulated spectra confirms the strong overlap of the signals of the different oxygen species. Figure 13 shows, as an example, the deconvoluted (BO, NBO, and TO) spectra of N13M13 glass, calculated with the SM1 potential.

The ^{17}O 2D MQMAS NMR spectra allow for an in-depth description of the structure and their correct reproduction can give valuable insights into structural features of the glasses. Figure 14 shows a comparison between experimental[24] ^{17}O 2D MQMAS NMR spectra and simulated ones with the three studied potentials for N26M0, N13M13, and N0M12 glasses. The spectra of all the studied glasses can be found in Figure S21.

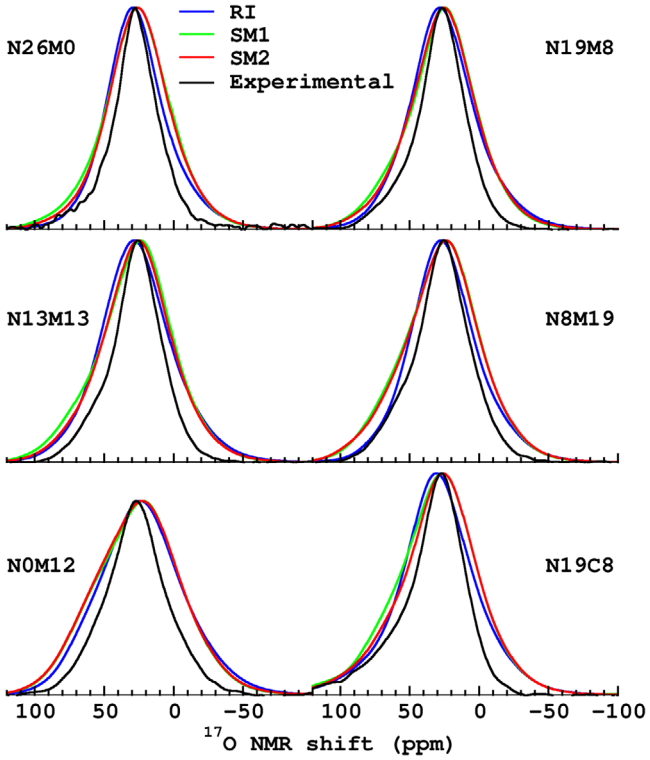

FIGURE 12 Experimental[24] and simulated ^{17}O MAS NMR spectra of the studied glasses.

The SM potentials, and especially SM2, seem to better reproduce the shape of the spectra. In particular, the Si–O–B and B–O–B contributions are better reproduced with the polarizable potentials, and the separations between each part of the spectra are more visible. Moreover, also the Si–O–M part, with M = Al, Mg, Na, and Ca, is better reproduced by the SM1 and SM2 potentials. SM2 seems to perform slightly better. SM1 shows a contribution at around −70 ppm in the isotropic chemical shift scale that is not present in the experimental spectra. MQMAS spectra reported in Figure S22 do not allow to distinguish the BO/NBO contributions.

The isotropic chemical shift projections of the ^{17}O MQMAS NMR spectra are reported in Figure S23. Even in this case, the SM potentials perform better than the RI one. The deconvolution of the isotropic projection (Figure S24) allows to assign the peaks of the spectra to specific contributions, confirming the increasing Si–O–Si content, and highlights again the strong overlap of the signals, and in particular of the Si–O–Al and Si–NBO ones.

3.3.4 | ^{29}Si MAS NMR spectra

^{29}Si NMR spectra are often used to determine the Q^n population of the silicon atoms.[83] Unfortunately, the complex composition of the studied glasses makes the interpretation of the spectra more difficult as the isotropic chemical shift depends also on the nature and amount of second neighbor atoms. In particular, for a given Q^n species, other network formers (i.e., Al, B, …) tend to move the peak to higher chemical shifts,[81,84] and the opposite effect is given by modifiers.[85,86] Our simulations, as shown in Tables S12 and S13, confirm these general trends. A broader signal is usually related to a more disordered silicon environment, given by a larger Q^n distribution or an increase for Si–O–X (X = Al, B) bonds.[87] In general, a more polymerized silicon network (so higher Q^n species), gives lower chemical shift values. This is shown in Figure S25, where the spectra of the different Q^n species of N13M13 glass obtained with SM1 potential are reported.

Figure 15 shows the comparison between simulated[24] and experimental ^{29}Si MAS NMR spectra. The simulation of the ^{29}Si NMR spectra can be very helpful in the interpretation of experimental data and for the validation of the simulated model, from which important structural features can be extracted, such as Q^n distribution and second neighbor atoms.

The experiments show a broadening and a shift of the peak to lower chemical shifts when magnesium content increases. This trend is well reproduced by all the potentials. MD structures present a broader Q^n distribution of silicon, which explains the broadening of the signal. The shift over more negative values could be explained by the high-field strength of Mg, which, even if it is usually considered a modifier element, could be low coordinated and act as an intermediate network former[15,21,22,88] (like Al), giving more polymerization of the silicon network.

The strong decreases in the chemical shift of N0M12 can be explained by the high polymerization of Si in this glass, for which all the potentials predict 93%–95% Si[Q^4]. The experimental data are shifted to lower values with respect to the simulations. This is probably due to an underestimation of the amount of Si–O–Si bridges in the simulated structures with respect to the experiments. In fact, Q^4 units connected to silicon, in vitreous silica, give a spectrum that is approximately centered at −110 ppm. Simulations show that N8M19 and N0M12 could have a clustering of Si-rich regions (see Section 3.2.1) if compared with a complete random structure and this could explain the shift toward lower chemical shifts.

4 | CONCLUSION

Three MD potentials have been assessed for the simulation from first-principles of ^{11}B, ^{17}O, ^{23}Na, ^{25}Mg, ^{27}Al, and ^{29}Si MAS NMR spectra, structural features, and neutron diffraction pattern of a series of aluminoborosilicate glasses where Mg oxide gradually substitutes Na oxide.

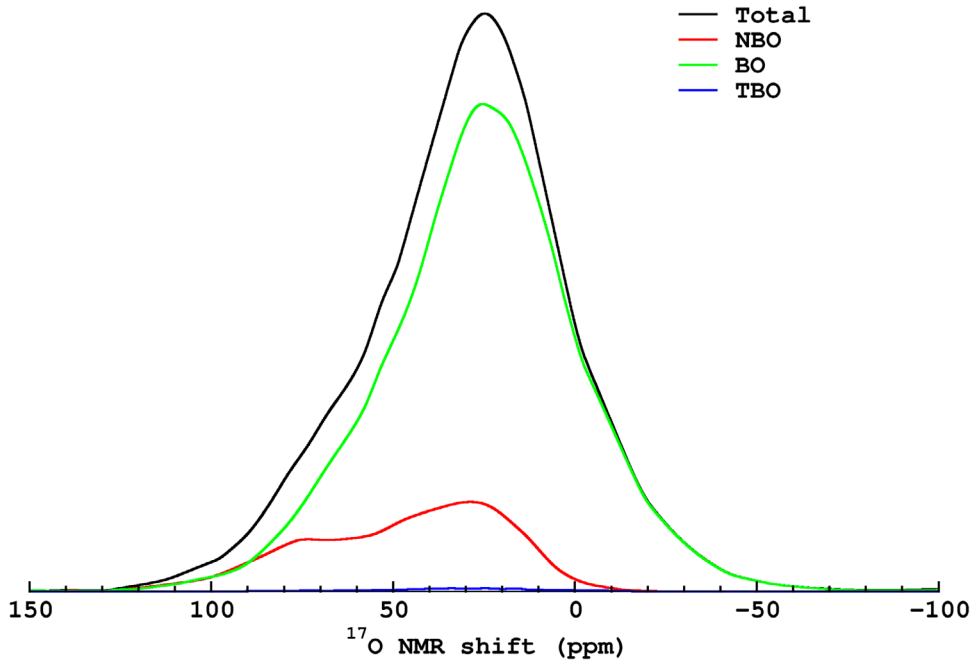

FIGURE 13 ^{17}O MAS NMR spectra of N13M13 glass simulated with SM1 FF. The NBO, BO, and TBO contributions to the total spectrum are also reported.

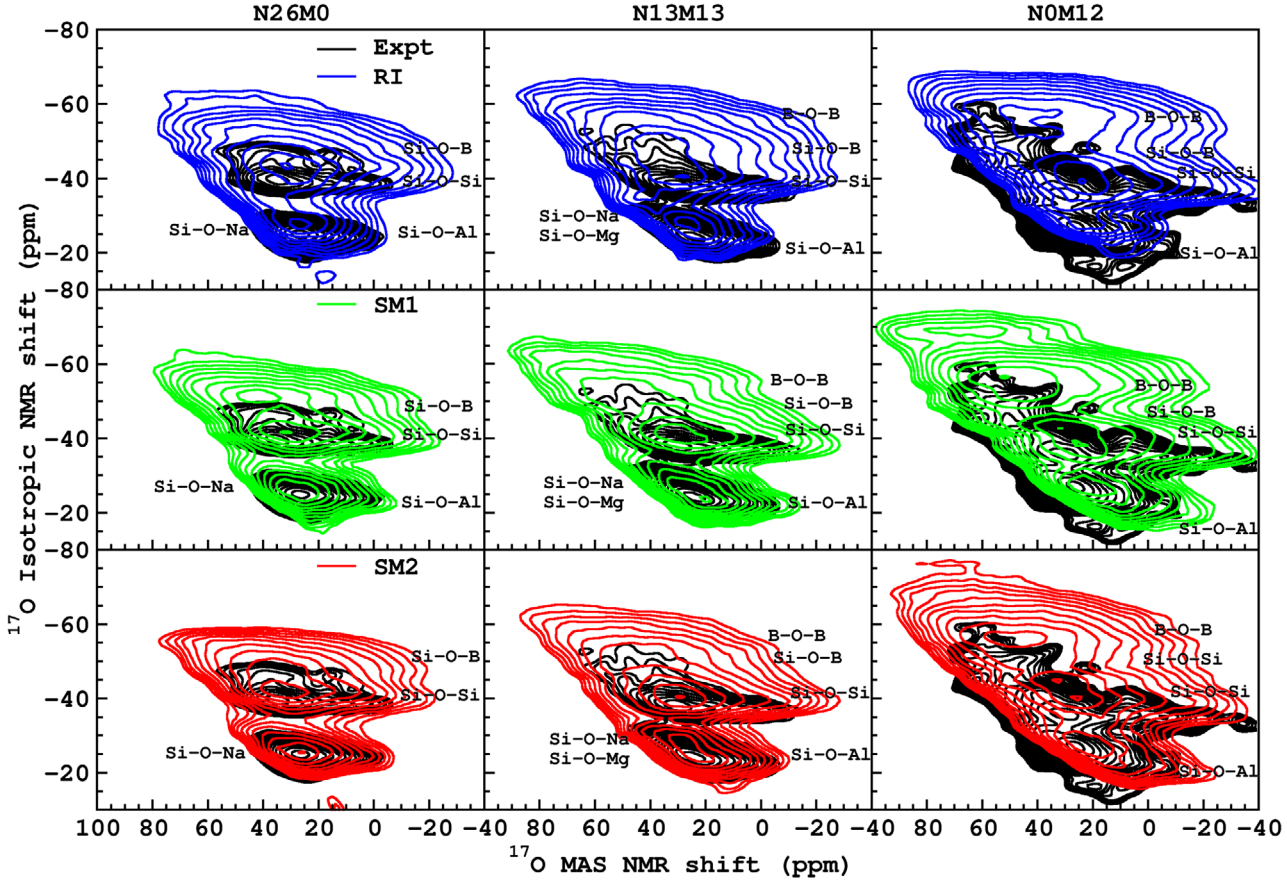

FIGURE 14 Experimental[24] and simulated ^{17}O MQMAS NMR spectra of N26M0, N13M13, and N0M12 glasses.

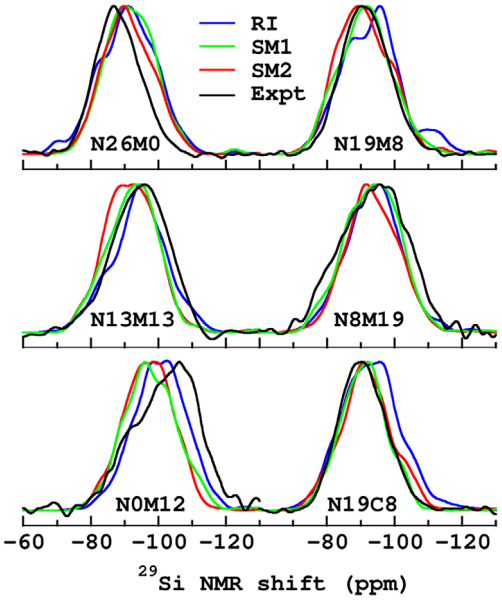

FIGURE 15 Experimental[24] and simulated ^{29}Si MAS NMR spectra of the studied glasses.

The first potential (RI) is based on the rigid-ion model and was developed by Wang et al.[27] using Coulomb–Buckingham two-body interactions and has parameters that do not depend on the composition. The other two potentials are based on the core–shell approach proposed by Dick and Overhauser[49] and differ in the (composition independent) B–O interaction parameters. The latter has been originally developed by Stevensson et al.[36] (SM1 potential) and subsequently refined by Pedone et al.[37] to better simulate glasses with high BO_4 content (SM2 potential).

All the NMR spectra simulated with SM1 and SM2 gives a much better agreement with experiments, thus validating the simulated structures. In particular, ^{17}O MQMAS NMR spectra are better reproduced by SM2 potential, while ^{11}B MAS NMR spectra by SM1.

SM1 predicts the N_4 fraction in the glass series accurately, while RI largely overestimates N_4. SM2 perfectly predicts N_4 only for N26M0 (where BO_4 is predominant) and then overestimates. Furthermore, RI always gives a non-negligible amount of Al in high coordination state (AlO_5) while SM potentials predict very low values.

If the RI potential predicts a non-negligible amount of Al–NBO linkages and the highest BO_4–NBO bonds, SM potential do not predict NBO on Al and minor percentages of NBO in BO_4, especially with the SM2 modified parameters.

The coordination number of Mg and its distance to oxygen atoms obtained from the simulations would suggest a behavior that is in between a network modifier (like Na) and an intermediate network former (like Al) making the boundary between these two categories less clear than expected. Further studies should be done to clarify the dependence of the Mg behavior on the composition of the glass. Magnesium atoms lay closer to B with respect to Si and especially Al, this is particularly true using the SM potentials, and can be the cause of the formation of the higher coordinated Al in Na-free glass, where no sodium atoms can compensate AlO_4^- units. Furthermore the simulations confirm the possible silicon segregation in Si-rich silicate (with dominant Si–O–Si linkages) regions when Mg becomes predominant with respect to Na. This phenomenon is more pronounced when only Mg is present.

ACKNOWLEDGMENTS

This study was supported by the French Alternative Energies and Atomic Energy Commission (CEA) and Electricité de France (EDF). This work was granted access to the HPC resources of TGCC under the allocation DARI-A0070906303 (2019) and DARI-A0110906303 (2021) attributed by GENCI (Grand Equipement National de Calcul Intensif).

ORCID

Marco Bertani https://orcid.org/0000-0002-0434-1238
Nicolas Bisbrouck https://orcid.org/0000-0003-1903-3032
Jean-Marc Delaye https://orcid.org/0000-0002-1311-642X
Alfonso Pedone https://orcid.org/0000-0003-3772-7222
Thibault Charpentier https://orcid.org/0000-0002-3034-1389

REFERENCES

1. Kaur G, Sharma P, Kumar V, Singh K. Assessment of in vitro bioactivity of SiO_2-BaO-ZnO-B_2O_3-Al_2O_3 glasses: an optico-analytical approach. Mater Sci Eng C. 2012;32(7):1941–7. https://doi.org/10.1016/j.msec.2012.05.034
2. Kato Y, Yamazaki H, Watanabe T, Saito K, Ikushima AJ. Early stage of phase separation in aluminoborosilicate glass for liquid crystal display substrate. J Am Ceram Soc. 2005;88(2):473–7. https://doi.org/10.1111/j.1551-2916.2005.00079.x
3. Yamashita H, Inoue K, Nakajin T, Inoue H, Maekawa T. Nuclear magnetic resonance studies of 0.139MO (or M'_2O)·0.673SiO_2·(0.188−x)Al_2O_3·xB_2O_3 (M = Mg, Ca, Sr and Ba, M′ = Na and K) glasses. J Non-Cryst Solids. 2003;331(1):128–36. https://doi.org/10.1016/j.jnoncrysol.2003.08.086
4. Jensen WB. The origin of Pyrex. J Chem Educ. 2006;83(5):692. https://doi.org/10.1021/ed083p692
5. Gerasimov VV, Spirina OV. Coordination state of boron and aluminum in low-alkali aluminoborosilicate glasses. Glass Ceram. 2004;61(5):168–70. https://doi.org/10.1023/B:GLAC.0000043083.36991.df
6. Li H, Hrma P, Vienna JD, Qian M, Su Y, Smith DE. Effects of Al_2O_3, B_2O_3, Na_2O, and SiO_2 on nepheline formation in

borosilicate glasses: chemical and physical correlations. J Non-Cryst Solids. 2003;331(1):202–16. https://doi.org/10.1016/j.jnoncrysol.2003.08.082

7. Boizot B, Ollier N, Olivier F, Petite G, Ghaleb D, Malchukova E. Irradiation effects in simplified nuclear waste glasses. Nucl Instrum Methods Phys Res B. 2005;240(1):146–51. https://doi.org/10.1016/j.nimb.2005.06.105
8. Ollier N, Charpentier T, Boizot B, Petite G. A structural approach by MAS NMR spectroscopy of mechanisms occurring under β-irradiation in mixed alkali aluminoborosilicate glasses. J Phys Condens Matter. 2004;16(43):7625–35. https://doi.org/10.1088/0953-8984/16/43/006
9. Besmann TM, Spear KE. Thermochemical modeling of oxide glasses. J Am Ceram Soc. 2002;85(12):2887–94. https://doi.org/10.1111/j.1151-2916.2002.tb00552.x
10. Jan A, Delaye J-M, Gin S, Kerisit S. Molecular dynamics simulation of ballistic effects in simplified nuclear waste glasses. J Non-Cryst Solids. 2019;505:188–201. https://doi.org/10.1016/j.jnoncrysol.2018.11.021
11. Quintas A, Caurant D, Majérus O, Charpentier T, Dussossoy J-L. Effect of the nature of alkali and alkaline-earth oxides on the structure and crystallization of an aluminoborosilicate glass developed to immobilize highly concentrated nuclear waste solutions. arXiv. 2009. https://doi.org/10.48550/arXiv.0912.1576
12. Quintas A, Caurant D, Majérus O, Charpentier T, Dussossoy J-L. Effect of compositional variations on charge compensation of AlO_4 and BO_4 entities and on crystallization tendency of a rare-earth-rich aluminoborosilicate glass. Mater Res Bull. 2009;44(9):1895–8. https://doi.org/10.1016/j.materresbull.2009.05.009
13. Gin S, Abdelouas A, Criscenti LJ, Ebert WL, Ferrand K, Geisler T, et al. An international initiative on long-term behavior of high-level nuclear waste glass. Mater Today. 2013;16(6):243–8. https://doi.org/10.1016/j.mattod.2013.06.008
14. Backhouse DJ, Corkhill CL, Hyatt NC, Hand RJ. Investigation of the role of Mg and Ca in the structure and durability of aluminoborosilicate glass. J Non-Cryst Solids. 2019;512:41–52. https://doi.org/10.1016/j.jnoncrysol.2019.03.003
15. Guo R, Brigden CT, Gin S, Swanton SW, Farnan I. The effect of magnesium on the local structure and initial dissolution rate of simplified UK Magnox waste glasses. J Non-Cryst Solids. 2018;497:82–92. https://doi.org/10.1016/j.jnoncrysol.2018.03.002
16. Harrison MT. The effect of composition on short- and long-term durability of UK HLW glass. Procedia Mater Sci. 2014;7:186–92. https://doi.org/10.1016/j.mspro.2014.10.025
17. Thien BMJ, Godon N, Ballestero A, Gin S, Ayral A. The dual effect of Mg on the long-term alteration rate of AVM nuclear waste glasses. J Nucl Mater. 2012;427(1):297–310. https://doi.org/10.1016/j.jnucmat.2012.05.025
18. Vernaz É, Bruezière J. History of nuclear waste glass in France. Procedia Mater Sci. 2014;7:3–9. https://doi.org/10.1016/j.mspro.2014.10.002
19. Barlow ST, Fisher AJ, Bailey DJ, Blackburn LR, Stennett MC, Hand RJ, et al. Thermal treatment of nuclear fuel-containing Magnox sludge radioactive waste. J Nucl Mater. 2021;552:152965. https://doi.org/10.1016/j.jnucmat.2021.152965
20. Souza MT, Crovace MC, Schröder C, Eckert H, Peitl O, Zanotto ED. Effect of magnesium ion incorporation on the thermal stability, dissolution behavior and bioactivity in Bioglass-derived glasses. J Non-Cryst Solids. 2013;382:57–65. https://doi.org/10.1016/j.jnoncrysol.2013.10.001
21. Pedone A, Malavasi G, Menziani MC, Segre U, Cormack AN. Role of magnesium in soda-lime glasses: insight into structural, transport, and mechanical properties through computer simulations. J Phys Chem C. 2008;112(29):11034–41. https://doi.org/10.1021/jp8016776
22. Watts SJ, Hill RG, O'Donnell MD, Law RV. Influence of magnesia on the structure and properties of bioactive glasses. J Non-Cryst Solids. 2010;356(9):517–24. https://doi.org/10.1016/j.jnoncrysol.2009.04.074
23. Aréna H, Rébiscoul D, Podor R, Garcès E, Cabie M, Mestre J-P, et al. Impact of Fe, Mg and Ca elements on glass alteration: interconnected processes. Geochim Cosmochim Acta. 2018;239:420–45. https://doi.org/10.1016/j.gca.2018.08.007
24. Bisbrouck N, Bertani M, Angeli F, Charpentier T, de Ligny D, Delaye J-M, et al. Impact of magnesium on the structure of aluminoborosilicate glasses: a solid-state NMR and Raman spectroscopy study. J Am Ceram Soc. 2021;104(9):4518–36. https://doi.org/10.1111/jace.17876
25. Pedone A, Malavasi G, Menziani MC. Computational insight into the effect of CaO/MgO substitution on the structural properties of phospho-silicate bioactive glasses. J Phys Chem C. 2009;113(35):15723–30. https://doi.org/10.1021/jp904131t
26. Du J, Cormack AN. The medium range structure of sodium silicate glasses: a molecular dynamics simulation. J Non-Cryst Solids. 2004;349:66–79. https://doi.org/10.1016/j.jnoncrysol.2004.08.264
27. Wang M, Anoop Krishnan NM, Wang B, Smedskjaer MM, Mauro JC, Bauchy M. A new transferable interatomic potential for molecular dynamics simulations of borosilicate glasses. J Non-Cryst Solids. 2018;498:294–304. https://doi.org/10.1016/j.jnoncrysol.2018.04.063
28. Bertani M, Menziani MC, Pedone A. Improved empirical force field for multicomponent oxide glasses and crystals. Phys Rev Mater. 2021;5(4):045602. https://doi.org/10.1103/PhysRevMaterials.5.045602
29. Tuheen MI, Deng L, Du J. A comparative study of the effectiveness of empirical potentials for molecular dynamics simulations of borosilicate glasses. J Non-Cryst Solids. 2021;553:120413. https://doi.org/10.1016/j.jnoncrysol.2020.120413
30. Angeli F, Delaye J-M, Charpentier T, Petit J-C, Ghaleb D, Faucon P. Influence of glass chemical composition on the Na–O bond distance: a ^{23}Na 3Q-MAS NMR and molecular dynamics study. J Non-Cryst Solids. 2000;276(1):132–44. https://doi.org/10.1016/S0022-3093(00)00259-3
31. Du J, Benmore CJ, Corrales R, Hart RT, Weber JKR. A molecular dynamics simulation interpretation of neutron and X-ray diffraction measurements on single phase Y_2O_3–Al_2O_3glasses. J Phys Condens Matter. 2009;21(20):205102. https://doi.org/10.1088/0953-8984/21/20/205102
32. Lodesani F, Menziani MC, Hijiya H, Takato Y, Urata S, Pedone A. Structural origins of the mixed alkali effect in alkali aluminosilicate glasses: molecular dynamics study and its assessment. Sci Rep. 2020;10(1):2906. https://doi.org/10.1038/s41598-020-59875-7
33. Pedone A, Bertani M, Brugnoli L, Pallini A. Interatomic potentials for oxide glasses: past, present, and future. J Non-

Cryst Solids X. 2022;15:100115. https://doi.org/10.1016/j.nocx.2022.100115
34. Lee K-H, Yang Y, Ziebarth B, Mannstadt W, Davis MJ, Mauro JC. Evaluation of classical interatomic potentials for molecular dynamics simulations of borosilicate glasses. J Non-Cryst Solids. 2020;528:119736. https://doi.org/10.1016/j.jnoncrysol.2019.119736
35. Fortino M, Berselli A, Stone-Weiss N, Deng L, Goel A, Du J, et al. Assessment of interatomic parameters for the reproduction of borosilicate glass structures via DFT-GIPAW calculations. J Am Ceram Soc. 2019;102(12):7225–43. https://doi.org/10.1111/jace.16655
36. Stevensson B, Yu Y, Edén M. Structure–composition trends in multicomponent borosilicate-based glasses deduced from molecular dynamics simulations with improved B–O and P–O force fields. Phys Chem Chem Phys. 2018;20(12):8192–209. https://doi.org/10.1039/C7CP08593A
37. Stone-Weiss N, Bradtmüller H, Fortino M, Bertani M, Youngman RE, Pedone A, et al. Combined experimental and computational approach toward the structural design of borosilicate-based bioactive glasses. J Phys Chem C. 2020;124(32):17655–74. https://doi.org/10.1021/acs.jpcc.0c04470
38. Shih Y-T, Sundararaman S, Ispas S, Huang L. New interaction potentials for alkaline earth silicate and borate glasses. *ArXiv210208733 Cond-Mat*. 2021.
39. Sundararaman S, Huang L, Ispas S, Kob W. New interaction potentials for borate glasses with mixed network formers. J Chem Phys. 2020;152(10):104501. https://doi.org/10.1063/1.5142605
40. Pacaud F, Delaye J-M, Charpentier T, Cormier L, Salanne M. Structural study of Na_2O–B_2O_3–SiO_2 glasses from molecular simulations using a polarizable force field. J Chem Phys. 2017;147(16):161711. https://doi.org/10.1063/1.4992799
41. Kieu L-H, Delaye J-M, Cormier L, Stolz C. Development of empirical potentials for sodium borosilicate glass systems. J Non-Cryst Solids. 2011;357(18):3313–21. https://doi.org/10.1016/j.jnoncrysol.2011.05.024
42. Inoue H, Masuno A, Watanabe Y. Modeling of the structure of sodium borosilicate glasses using pair potentials. J Phys Chem B. 2012;116(40):12325–31. https://doi.org/10.1021/jp3038126
43. Yun YH, Bray PJ. Nuclear magnetic resonance studies of the glasses in the system Na_2O B_2O_3 SiO_2. J Non-Cryst Solids. 1978;27(3):363–80. https://doi.org/10.1016/0022-3093(78)90020-0
44. Dell WJ, Bray PJ, Xiao SZ. ^{11}B NMR studies and structural modeling of Na_2O B_2O_3 SiO_2 glasses of high soda content. J Non-Cryst Solids. 1983;58(1):1–16. https://doi.org/10.1016/0022-3093(83)90097-2
45. Manara D, Grandjean A, Neuville DR. Structure of borosilicate glasses and melts: a revision of the Yun, Bray and Dell model. J Non-Cryst Solids. 2009;355(50–51):2528–31. https://doi.org/10.1016/j.jnoncrysol.2009.08.033
46. Bertani M, Pallini A, Cocchi M, Menziani MC, Pedone A. A new self-consistent empirical potential model for multicomponent borate and borosilicate glasses. J Am Ceram Soc. 2022;105(12):7254–71. https://doi.org/10.1111/jace.18681
47. Bisbrouck N, Micoulaut M, Delaye J-M, Bertani M, Charpentier T, Gin S, et al. Influence of magnesium on the structure of complex multicomponent silicates: insights from molecular simulations and neutron scattering experiments. J Phys Chem B. 2021;125(42):11761–76. https://doi.org/10.1021/acs.jpcb.1c06990
48. Charpentier T, Cristina Menziani M, Pedone A. Computational simulations of solid state NMR spectra : a new era in structure determination of oxide glasses. RSC Adv. 2013;3(27):10550–78. https://doi.org/10.1039/C3RA40627J
49. Dick BG, Overhauser AW. Theory of the dielectric constants of alkali halide crystals. Phys Rev. 1958;112(1):90–103. https://doi.org/10.1103/PhysRev.112.90
50. Tilocca A, de Leeuw NH, Cormack AN. Shell-model molecular dynamics calculations of modified silicate glasses. Phys Rev B. 2006;73(10):104209. https://doi.org/10.1103/PhysRevB.73.104209
51. Pedone A, Gambuzzi E, Malavasi G, Menziani MC. First-principles simulations of the ^{27}Al and ^{17}O solid-state NMR spectra of the $CaAl_2Si_3O_{10}$ glass. Theor Chem Acc. 2012;131(3):1147. https://doi.org/10.1007/s00214-012-1147-5
52. Gambuzzi E, Pedone A, Menziani MC, Angeli F, Caurant D, Charpentier T. Probing silicon and aluminium chemical environments in silicate and aluminosilicate glasses by solid state NMR spectroscopy and accurate first-principles calculations. Geochim Cosmochim Acta. 2014;125:170–85. https://doi.org/10.1016/j.gca.2013.10.025
53. Todorov IT, Smith W, Trachenko K, Dove MT. DL_POLY_3: new dimensions in molecular dynamics simulations via massive parallelism. J Mater Chem. 2006;16(20):1911–8. https://doi.org/10.1039/B517931A
54. Charpentier T, Kroll P, Mauri F. First-principles nuclear magnetic resonance structural analysis of vitreous silica. J Phys Chem C. 2009;113(18):7917–29. https://doi.org/10.1021/jp900297r
55. Hutter J, Iannuzzi M, Schiffmann F, VandeVondele J. cp2k: atomistic simulations of condensed matter systems. WIREs Comput Mol Sci. 2014;4(1):15–25. https://doi.org/10.1002/wcms.1159
56. Guillot B, Sator N. A computer simulation study of natural silicate melts. Part I: Low pressure properties. Geochim Cosmochim Acta. 2007;71(5):1249–65. https://doi.org/10.1016/j.gca.2006.11.015
57. Allen MP, Tildesley D. Computer Simulation of Liquids. 1988. https://doi.org/10.2307/2938686
58. Nosé S. A unified formulation of the constant temperature molecular dynamics methods. J Chem Phys. 1984;81(1):511–9. https://doi.org/10.1063/1.447334
59. Hoover WG. Canonical dynamics: equilibrium phase-space distributions. Phys Rev A. 1985;31(3):1695–7. https://doi.org/10.1103/PhysRevA.31.1695
60. Tilocca A, Cormack AN, de Leeuw NH. The structure of bioactive silicate glasses: new insight from molecular dynamics simulations. Chem Mater. 2007;19(1):95–103. https://doi.org/10.1021/cm061631g
61. Yu Y, Stevensson B, Edén M. Medium-range structural organization of phosphorus-bearing borosilicate glasses revealed by advanced solid-state NMR experiments and MD simulations: consequences of B/Si substitutions. J Phys Chem B. 2017;121(41):9737–52. https://doi.org/10.1021/acs.jpcb.7b06654
62. Pickard CJ, Mauri F. All-electron magnetic response with pseudopotentials: NMR chemical shifts. Phys Rev B. 2001;63(24):245101. https://doi.org/10.1103/PhysRevB.63.245101
63. Bonhomme C, Gervais C, Babonneau F, Coelho C, Pourpoint F, Azaïs T, et al. First-principles calculation of NMR parameters using the gauge including projector augmented wave method: a chemist's point of view. Chem Rev. 2012;112(11):5733–79. https://doi.org/10.1021/cr300108a

64. Kresse G, Furthmüller J. Efficient iterative schemes for ab initio total-energy calculations using a plane-wave basis set. Phys Rev B. 1996;54(16):11169–86. https://doi.org/10.1103/PhysRevB.54.11169
65. Perdew JP, Burke K, Ernzerhof M. Generalized gradient approximation made simple. Phys Rev Lett. 1996;77(18):3865–8. https://doi.org/10.1103/PhysRevLett.77.3865
66. Jaworski A, Charpentier T, Stevensson B, Edén M. Scandium and yttrium environments in aluminosilicate glasses unveiled by $^{45}Sc/^{89}Y$ NMR spectroscopy and DFT calculations: what structural factors dictate the chemical shifts? J Phys Chem C. 2017;121(34):18815–29. https://doi.org/10.1021/acs.jpcc.7b05471
67. Profeta M, Benoit M, Mauri F, Pickard CJ. First-principles calculation of the ^{17}O NMR parameters in Ca oxide and Ca aluminosilicates: the partially covalent nature of the Ca—O bond, a challenge for density functional theory. J Am Chem Soc. 2004;126(39):12628–35. https://doi.org/10.1021/ja0490830
68. Soleilhavoup A, Delaye J-M, Angeli F, Caurant D, Charpentier T. Contribution of first-principles calculations to multinuclear NMR analysis of borosilicate glasses. Magn Reson Chem. 2010;48(S1):S159–70. https://doi.org/10.1002/mrc.2673
69. Sørensen SS, Johra H, Mauro JC, Bauchy M, Smedskjaer MM. Boron anomaly in the thermal conductivity of lithium borate glasses. Phys Rev Mater. 2019;3(7):075601. https://doi.org/10.1103/PhysRevMaterials.3.075601
70. Doweidar H. Consideration of the boron oxide anomaly. J Mater Sci. 1990;25(1):253–8. https://doi.org/10.1007/BF00544216
71. Gaafar MS, Marzouk SY, Zayed HA, Soliman LI, Serag El-Deen AH. Structural studies and mechanical properties of some borate glasses doped with different alkali and cobalt oxides. Curr Appl Phys. 2013;13(1):152–8. https://doi.org/10.1016/j.cap.2012.07.007
72. Bray PJ. Structural models for borate glasses. J Non-Cryst Solids. 1985;75(1):29–36. https://doi.org/10.1016/0022-3093(85)90198-X
73. Verhoef AH, den Hartog HW. Structure and dynamics of alkali borate glasses: a molecular dynamics study. J Non-Cryst Solids. 1995;182(3):235–47. https://doi.org/10.1016/0022-3093(94)00554-0
74. Stebbins JF, Dubinsky EV, Kanehashi K, Kelsey KE. Temperature effects on non-bridging oxygen and aluminum coordination number in calcium aluminosilicate glasses and melts. Geochim Cosmochim Acta. 2008;72(3):910–25. https://doi.org/10.1016/j.gca.2007.11.018
75. Thompson LM, Stebbins JF. Non-stoichiometric non-bridging oxygens and five-coordinated aluminum in alkaline earth aluminosilicate glasses: effect of modifier cation size. J Non-Cryst Solids. 2012;358(15):1783–9. https://doi.org/10.1016/j.jnoncrysol.2012.05.022
76. Neuville DR, Cormier L, Montouillout V, Florian P, Millot F, Rifflet J-C, et al. Amorphous materials: properties, structure, and durability: structure of Mg- and Mg/Ca aluminosilicate glasses: ^{27}Al NMR and Raman spectroscopy investigations. Am Mineral. 2008;93(11–12):1721–31. https://doi.org/10.2138/am.2008.2867
77. Loewenstein W. The distribution of aluminum in the tetrahedra of silicates and aluminates. Am Mineral. 1954;39(1–2):92–6.
78. Wright AC. Borate structures: crystalline and vitreous. Phys Chem Glass. 2010;51(1):1–39.
79. Abe T. Borosilicate glasses. J Am Ceram Soc. 1952;35(11):284–99. https://doi.org/10.1111/j.1151-2916.1952.tb13051.x
80. Angeli F, Villain O, Schuller S, Charpentier T, de Ligny D, Bressel L, et al. Effect of temperature and thermal history on borosilicate glass structure. Phys Rev B. 2012;85(5):054110. https://doi.org/10.1103/PhysRevB.85.054110
81. Angeli F, Charpentier T, De Ligny D, Cailleteau C. Boron speciation in soda-lime borosilicate glasses containing zirconium. J Am Ceram Soc. 2010;93(9):2693–704. https://doi.org/10.1111/j.1551-2916.2010.03771.x
82. Bradtmüller H, Uesbeck T, Eckert H, Murata T, Nakane S, Yamazaki H. Structural origins of crack resistance on magnesium aluminoborosilicate glasses studied by solid-state NMR. J Phys Chem C. 2019;123(24):14941–54. https://doi.org/10.1021/acs.jpcc.9b03600
83. Maekawa H, Maekawa T, Kawamura K, Yokokawa T. The structural groups of alkali silicate glasses determined from ^{29}Si MAS-NMR. J Non-Cryst Solids. 1991;127(1):53–64. https://doi.org/10.1016/0022-3093(91)90400-Z
84. Amoureux J-P, Fernandez C, Steuernagel S. Z filtering in MQMAS NMR. J Magn Reson A. 1996;123(1):116–8. https://doi.org/10.1006/jmra.1996.0221
85. Murdoch JB, Stebbins JF, Carmichael ISE. High-resolution ^{29}Si NMR study of silicate and aluminosilicate glasses: the effect of network-modifying cations. Am Mineral. 1985;70(3–4):332–43.
86. Magi M, Lippmaa E, Samoson A, Engelhardt G, Grimmer AR. Solid-state high-resolution silicon-29 chemical shifts in silicates. J Phys Chem. 1984;88(8):1518–22. https://doi.org/10.1021/j150652a015
87. Nanba T, Nishimura M, Miura Y. A theoretical interpretation of the chemical shift of ^{29}Si NMR peaks in alkali borosilicate glasses. Geochim Cosmochim Acta. 2004;68(24):5103–11. https://doi.org/10.1016/j.gca.2004.05.042
88. Lograd M, Eckert H, Murata T, Nakane S, Yamazaki H. Structure-property relations in crack-resistant alkaline-earth aluminoborosilicate glasses studied by solid state NMR. J Am Ceram Soc. 2021;104(5):2250–67. https://doi.org/10.1111/jace.17629

SUPPORTING INFORMATION

Additional supporting information can be found online in the Supporting Information section at the end of this article.

How to cite this article: Bertani M, Bisbrouck N, Delaye J-M, Angeli F, Pedone A, Charpentier T. Effects of magnesium on the structure of aluminoborosilicate glasses: NMR assessment of interatomic potentials models for molecular dynamics. J Am Ceram Soc. 2023;106:5501–5521. https://doi.org/10.1111/jace.19157